magnetochemistry

MDPI

Article

Stability Analysis of Buoyancy Magneto Flow of Hybrid Nanofluid through a Stretchable/Shrinkable Vertical Sheet Induced by a Micropolar Fluid Subject to Nonlinear Heat Sink/Source

Umair Khan [1,2,*], Aurang Zaib [3], Anuar Ishak [1], Abeer M. Alotaibi [4], Sayed M. Eldin [5], Nevzat Akkurt [6], Iskandar Waini [7] and Javali Kotresh Madhukesh [8]

[1] Department of Mathematical Sciences, Faculty of Science and Technology, Universiti Kebangsaan Malaysia, UKM, Bangi 43600, Malaysia
[2] Department of Mathematics and Social Sciences, Sukkur IBA University, Sukkur 65200, Pakistan
[3] Department of Mathematical Sciences, Federal Urdu University of Arts, Science and Technology, Gulshan-e-Iqbal, Karachi 75300, Pakistan
[4] Department of Mathematics, Faculty of Science, University of Tabuk, P.O. Box 741, Tabuk 71491, Saudi Arabia
[5] Center of Research, Faculty of Engineering, Future University in Egypt, New Cairo 11835, Egypt
[6] Earth Rare Element and Research Center, Munzur University, Tunceli 62000, Turkey
[7] Fakulti Teknologi Kejuruteraan Mekanikal dan Pembuatan, Universiti Teknikal Malaysia Melaka, Hang Tuah Jaya, Melaka 76100, Malaysia
[8] Department of Studies and Research in Mathematics, Davangere University, Davangere 577002, India
* Correspondence: umairkhan@iba-suk.edu.pk

check for updates

Citation: Khan, U.; Zaib, A.; Ishak, A.; Alotaibi, A.M.; Eldin, S.M.; Akkurt, N.; Waini, I.; Madhukesh, J.K. Stability Analysis of Buoyancy Magneto Flow of Hybrid Nanofluid through a Stretchable/Shrinkable Vertical Sheet Induced by a Micropolar Fluid Subject to Nonlinear Heat Sink/Source. *Magnetochemistry* **2022**, *8*, 188. https://doi.org/10.3390/magnetochemistry8120188

Academic Editor: Kamil Gareev

Received: 14 November 2022
Accepted: 10 December 2022
Published: 14 December 2022

Publisher's Note: MDPI stays neutral with regard to jurisdictional claims in published maps and institutional affiliations.

Abstract: The utilization of hybrid nanofluids (HNs) to boost heat transfer is a promising area of study, and thus, numerous scientists, researchers, and academics have voiced their admiration and interest in this area. One of the main functions of nanofluids is their dynamic role in cooling small electrical devices such as microchips and associated gadgets. The major goal of this study is to perform an analysis of the buoyancy flow of a shrinking/stretching sheet, whilst considering the fascinating and practical uses of hybrid nanofluids. The influence of a nonlinear heat source/sink induced by a micropolar fluid is also inspected. Water-based alumina and copper nanoparticles are utilized to calculate the fine points of the fluid flow and the features of heat transfer. The governing equations are framed with acceptable assumptions and the required similarity transformations are used to turn the set of partial differential equations into ordinary differential equations. The bvp4c technique is used to solve the simplified equations. Dual solutions are presented for certain values of stretching/shrinking parameters as well as the mixed convective parameter. In addition, the shear stress coefficient in the first-branch solution (FBS) escalates and decelerates for the second-branch solution (SBS) with the superior impact of the magnetic parameter, the mass transpiration parameter, and the solid nanoparticles volume fraction, while the contrary behavior is seen in both (FB and SB) solutions for the larger values of the material parameter.

Keywords: hybrid nanofluid; micropolar fluid; nonlinear heat source/sink

1. Introduction

Fluids are crucial to the acceleration of the heat transport phenomenon in many industrial or engineering systems, including fuel cells, heat exchangers, and others. To overcome this problem, we require specialized fluids with high thermal conductivities because conventional fluids have poor thermal conductivities. The unique fluids are known as "nanofluids". Choi [1] was the first to propose the term "nanofluid". The superior thermal conductivity caused by the metallic nanometer-sized particles is a significant feature of nanofluids compared with conventional fluids such as oil, water, and glycerin.

Many scientists [2–8] have focused their studies on fluid flow and heat transfer issues when utilizing either nanofluids or regular fluids.

By combining two distinct types of nanoparticles to form a hybrid nanofluid, it is possible to further improve the thermal conductivity of single nanoparticles. Hybrid nanofluids (HNs) are the next generation of nanofluids with superior thermo-physical characteristics. Ghadikolaei et al. [9] claimed in their reports that the existence of binary HN may enhance the rate of heat transfer against normal nanofluids and also minimize the production cost, which is beneficial for organizations. They noticed that using platelet-shaped nanoparticles is much more efficient. According to Sundar et al. [10], hybrid nanofluids are used to prepare fluid flows to increase heat transfer rates while also increasing the thermal conductivity of the included nanofluids. Jamaluddin et al. [11] studied the buoyancy and magnetic impact of hybrid nanofluid towards a stagnation point past a porous stretching/shrinking sheet with heat sink/source. They observed multiple solutions for certain values of assisting and opposing flows. Khashi'ie et al. [12] inspected the HNF through a Riga plate with buoyancy effects. They performed the temporal stability test and found that the FBS is generally acceptable while the SBS is not acceptable. Waini et al. [13] modernized the features of the heat transporting phenomenon at the smooth flow through an HN across a permeable moving object and observed dual outcomes. They have shown that as the volume percentage of nanoparticles rises, the critical value at which the solution exists falls. Bakar et al. [14] utilized the hybrid nanofluid to examine the slip flow and heat transfer in a porous medium, past a porous shrinkable sheet with radiation influence. The results of their stability of solutions analysis indicated that the upper solution is stable while the lower solution is not. Recently, Salawu et al. [15] examined the impact of the magnetic field on the radiative flow of hybrid nanofluids incorporated in the Prandtl–Erying fluid across the interior solar parabolic collector. They also considered entropy generation and Joule heating effects to inspect the hybridization of the copper and cobalt ferrite nanoparticles of the aircraft wings.

The majority of production processes involve non-Newtonian fluids including polymeric suspensions, lubricants, colloidal solutions, paints, and biological fluids. Eringen [16] developed the concept of micropolar liquids to describe the inertial and microscopic characteristics of these liquids/fluids. Ishak et al. [17] examined the 2D flow near a stagnation point towards a shrinkable sheet induced by micropolar fluid and presented dual solutions. Bachok et al. [18] inspected the 2D stagnation point flow of a micropolar fluid past a shrinkable/stretchable sheet along with the convective boundary condition. The significance of micropolar fluid towards a stagnation point across the shrinking/stretching sheet was explored by Soid et al. [19]. They discussed a couple of practical applications which included the cooling of continuous strips in metallurgy and the stretching of plastic sheets in polymer extrusion. El-Aziz [20] examined the micropolar boundary layer flow and the properties of heat transfer related to a heated exponentially stretched continuous sheet that was cooled by a mixed convective flow. Applications in continuous casting, hot rolling, drawing, and extrusion are just a few examples of the practical processes in which heat transfer mechanisms are of relevance. Turkyilmazoglu [21] presented an exact solution of the buoyancy magneto flow and heat transfer incorporated in micropolar fluids through a cooled or heated stretchable sheet with heat generation/absorption. Ramadevi et al. [22] investigated the features of the heat transfer magneto flows of micropolar fluids along a stretching sheet, which plays a significant role in heat exchanges, transportation, the treatment of magnetic drugs, and fibre coating. On the other hand, non-Newtonian nanofluids are frequently found in a variety of commercial and technological applications, including tars, paints, glues, biological solutions, and melts of polymers. In recent times, Rafique et al. [23] used the Keller-box technique to inspect the micropolar fluid flow induced by nanofluid through an inclined surface of a sheet. The impact of heat source/sink on the dissipative flow of a micropolar fluid over a permeable stretchable heated sheet with erratic radiation upshot was studied by Sajid et al. [24]. They showed that the angular velocity uplifts due to the micro-rotation factor. Kausar et al. [25] scrutinized the impression of the viscous dissipation

on the thermal radiative flow over a permeable stretched sheet which was subject to a micropolar nanofluid in a porous medium. They discovered that the curves of velocity and temperature augment due to the micro rotation parameter.

The flow near an SPF expresses the liquid motion towards the stagnant region on a moving or stationary solid surface. The occurrence of the flow through the stagnation region happens commonly in engineering applications including wire drawing, polymer extrusions, and plastic sheets drawing, as well as in aerodynamics. Attia [26] examined the SPF of a micropolar liquid through a porous flat plate. The flow phenomenon close to the SP past a stretchable/shrinkable sheet was examined by Awaludin et al. [27]. They found double solutions for the shrinkable sheet and one solution for the stretchable sheet. Sadiq [28] scrutinized the impression of anisotropic slip on the magneto flow towards an SP containing nanofluid via a plate. He observed that the slip and magnetic effects decline the velocity profile. Zainal et al. [29] discussed the unsteady slip flow of an HN over a heated stretched/shrinkable sheet and presented two solutions. The results show that there are two possible solutions, which undoubtedly add to the stability analysis and validate the viability of the first solution. Recently, Mahmood et al. [30] utilized ternary nanofluids to investigate the unsteady slip flow close to the SP past a stretched/shrinkable sheet with heat absorption/generation.

The heat source/sink impact is vitally valuable to the industry. For example, the heat management component is largely responsible for end-product quality. After considering several aspects, researchers/scholars have evaluated the impression of heat absorption/generation on the dynamics of nanofluid flow with the features of heat transfer. For instance, Pal and Mandal [31] analyzed the impact of a magnetic field on the radiative flow of nanofluid induced by non-Newtonian fluid through a stretchy sheet with an irregular heat source/sink. They examined that the velocity decreases and the temperature increase in the presence/existence of nanofluid. The effects of the thermal radiation, heat absorption/generation, and the magnetic field on the dissipative flow of the Jeffrey nanofluid were investigated by Sharma and Gupta [32]. Additionally, Jamaludin et al. [33] investigated how the heat source/sink affected the flow of a mixed convective nanofluid over a movable surface while being affected by thermal radiation. They concluded that the impacts of heat sources, thermal radiation, and shrinking sheets may hasten the separation of the boundary layer. The significance of water-based hybrid alloy nanoparticles, Lorentz forces and Thomson and Troian slip impact over a stretching/shrinking cylinder with melting heat transfer has been examined by Khan et al. [34]. Recently, Khan et al. [35] examined the influence of an erratic heat sink/source on the buoyancy slip flow towards a slippery and stretchable sheet comprising nanofluid.

According to the review of the literature mentioned above, a hybrid nanofluid in the presence of non-Newtonian fluids has a lot of industrial applications because of its greater thermal performance compared with a typical heat transfer fluid. Thus, the present exploration is novel in five ways: (I) developing an important water-based hybrid micropolar nanofluid, i.e., Al_2O_3–Cu as a novel heat transfer fluid; (II) exploring a two-dimensional free time-dependent flow close to the stagnation point on a stretchable/shrinkable sheet using a single-phase model; (III) examining the magnetic radiation and irregular heat source/sink effects together; (IV) investigating the behavior of mixed convective or buoyancy forces; and (V) executing stability tests/assessments to check the stable solution in connecting to the dual solutions. To address these aims, the novelty of this research is to explore the impression of an irregular heat source/sink on the stagnation point buoyancy flow induced by micropolar hybrid nanofluids via a stretched/ shrinkable sheet along with magnetic and radiation effects. We believe that this problem has not yet been discussed. The flow problem was solved by using the bvp4c method, which is dependent on the finite difference approach. The impacts of the new parameters are explored numerically in the form of various tables, as well as being graphically represented. This research of buoyancy radiative flows induced by hybrid nanofluids with an irregular heat source/sink effect

through a shrinking/stretching surface is particularly important in food processes, polymer processing, biomedicine, aerodynamic heating, etc.

2. Description and Background of the Model

Let us consider the two-dimensional (2D) buoyancy or the mixed convective flow induced by micropolar hybrid nanofluids close to the SP over a porous vertical stretched or shrinking sheet. Figure 1 shows this flow configuration along with the wall surface velocity $u_w(x_s)$ and free stream velocity $u_{ex}(x_s)$, in which x_s and y_s indicate the Cartesian coordinates appraised along the stretched or contracted sheet and orthogonal to it, respectively. The hybrid nanofluid is made up of a water-based fluid and two different kinds of nanoparticles, copper (Cu) and alumina (Al_2O_3). Additionally, it is conceivable that the configuration of the fluid flow was also affected by the combined effects of thermal radiation and an irregular heat sink/source term. Another presumption is that the wall variable temperature and constant far-field temperature are signified by $T_w(x_s)$ and T_∞, respectively. The magnetic field measured to the sheet is assumed to have a constant strength B_0. Additionally, it is anticipated that the nanoparticles and water-based fluid would not slip and would be in thermal equilibrium. The single-phase method used in this hybrid nanofluid model assumes that the nanoparticles are homogenous in size and shape, and they do not interact with the surrounding fluid (see Sheremet et al. [36], Pang et al. [37], and Ebrahimi et al. [38]). This statement supports the adoption of the single-phase model in this study since it is practically applicable when the base fluid can be effectively disseminated and is thought to behave as a single fluid.

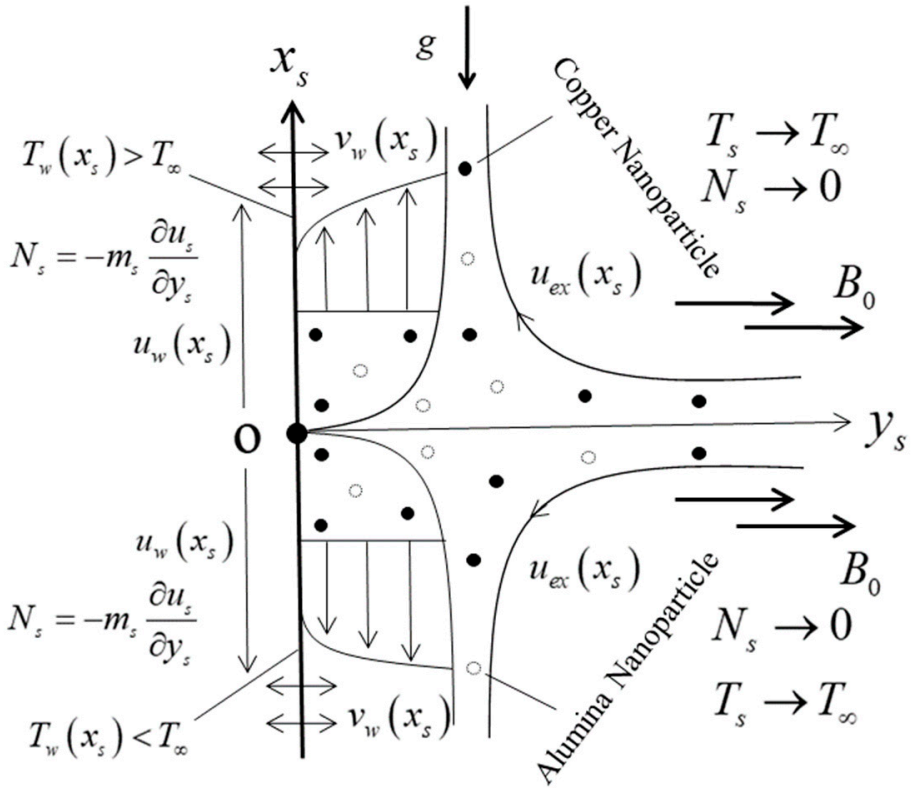

(**a**)

Figure 1. *Cont.*

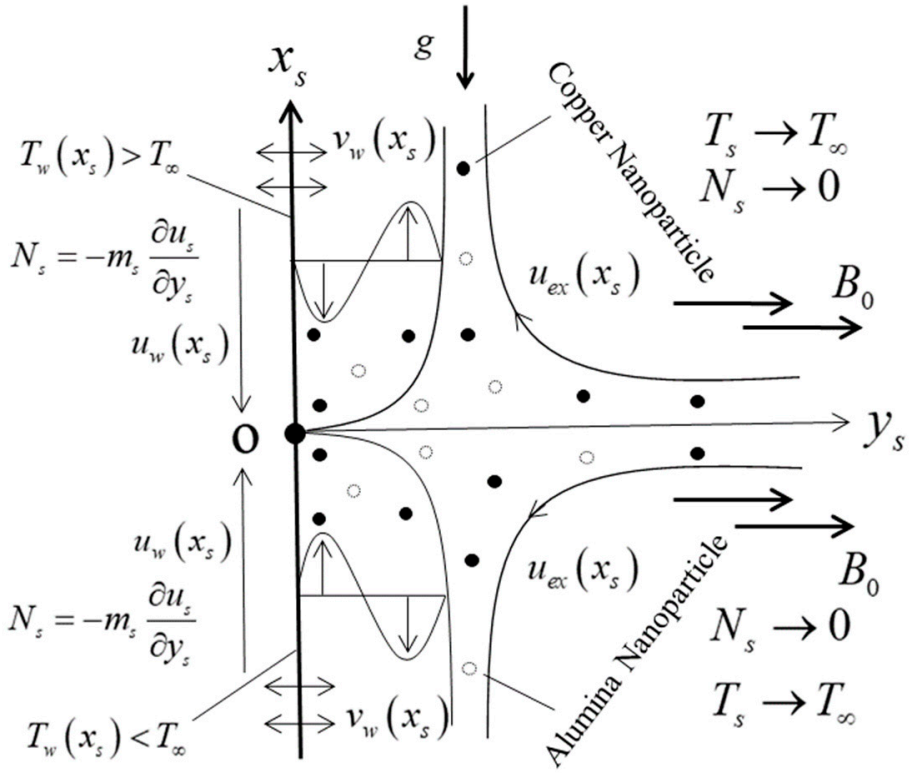

(b)

Figure 1. Physical model and coordinate system (**a**) Stretching sheet; (**b**) Shrinking sheet.

These hypotheses, along with the Boussinesq and boundary layer approximations, are taken into consideration while presenting the main governed equations in terms of PDEs as follows [23–25]:

$$\frac{\partial u_s}{\partial x_s} + \frac{\partial v_s}{\partial y_s} = 0, \tag{1}$$

$$\begin{aligned} u_s \frac{\partial u_s}{\partial x_s} + v_s \frac{\partial u_s}{\partial y_s} &= u_{ex} \frac{du_{ex}}{dx_s} + \frac{(\mu_{hnf} + \kappa_s)}{\rho_{hnf}} \frac{\partial^2 u_s}{\partial y_s^2} - \frac{\sigma_{hnf} B_0^2}{\rho_{hnf}} (u_s - u_{ex}) \\ &+ \frac{\kappa_s}{\rho_{hnf}} \frac{\partial N_s}{\partial y_s} + \frac{g(\rho\beta_T)_{hnf}}{\rho_{hnf}} (T_s - T_\infty), \end{aligned} \tag{2}$$

$$u_s \frac{\partial N_s}{\partial x_s} + v_s \frac{\partial N_s}{\partial y_s} = \frac{\left(\mu_{hnf} + \kappa_s/2\right)}{\rho_{hnf}} \frac{\partial^2 N_s}{\partial y_s^2} - \frac{\kappa_s}{j_s \rho_{hnf}} \left(2N_s + \frac{\partial u_s}{\partial y_s}\right), \tag{3}$$

$$u_s \frac{\partial T_s}{\partial x_s} + v_s \frac{\partial T_s}{\partial y_s} = \frac{k_{hnf}}{(\rho c_p)_{hnf}} \frac{\partial^2 T_s}{\partial y_s^2} - \frac{1}{(\rho c_p)_{hnf}} \frac{\partial q_r}{\partial y_s} + \frac{1}{(\rho c_p)_{hnf}} Q^{ccc}, \tag{4}$$

when the boundary conditions (BCs) are

$$\left.\begin{aligned} u_s = u_w(x_s),\ v_s = v_w(x_s),\ T_s = T_w(x_s),\ N_s = -m_s \tfrac{\partial u_s}{\partial y_s} \text{ at } y_s = 0, \\ u_s \to u_{ex}(x_s),\ T_s \to T_\infty,\ N_s \to 0 \text{ as } y_s \to \infty, \end{aligned}\right\} \tag{5}$$

where u_s and v_s indicate the elements of velocity in the posited x_s- and y_s- axes, respectively, T_s the temperature, g the acceleration caused by gravity, N_s the microrotation, κ_s the vortex viscosity, and j_s the micro-inertia density, $v_w(x_s)$ signifies the wall mass transpiration velocity with $v_w(x_s) > 0$ the case of blowing and $v_w(x_s) < 0$ the case of mass suction. According to these Refs. [39–41], m_s is steady with the given closed interval $[0, 1]$. The limiting case condition $m_s = 0$ is enforced in the case of strong concentration where the penetrating particles close to the contracted or stretched sheet do not swivel. The strong concentration

or the high level of focus and the slip-free situation $N_s = 0$ in the specified limiting instance are similarly matched. The microstructure particles have a negligibly small impact close to a sheet that is stretched or contracted, and this behavior is documented for the case when $m_s \neq 0$. Particularly, $m_s = 0.5$ indicates the weak concentration while the turbulent BLF is produced owing to the suitable case for $m_s = 1$.

Furthermore, σ_{hnf} represents the electrical conductivity of the hybrid nanofluid, μ_{hnf} denotes the absolute viscosity of the hybrid nanofluid, $(\rho\beta_T)_{hnf}$ represents the thermal expansion coefficient (TEC) of the hybrid nanofluid, ρ_{hnf} represents the density of the hybrid nanofluid, k_{hnf} represents the thermal conductivity (TCN) of the hybrid nanofluid, and $(\rho c_p)_{hnf}$ represents the specific heat capacitance of the hybrid nanofluid. The relations of these thermo-physical hybrid nanofluid symbols in the expression form are as follows (see Oztop and Abu-Nada [42]):

$$\frac{\mu_{hnf}}{\mu_f} = \frac{1}{(1-\varphi_{Cu}-\varphi_{Al_2O_3})^{2.5}}, \tag{6}$$

$$\frac{k_{hnf}}{k_f} = \frac{(C_a + C_b)}{(C_a + C_c)}, \tag{7}$$

where;

$C_a = \frac{(\varphi_{Cu}k_{Cu} + \varphi_{Al_2O_3}k_{Al_2O_3})}{\varphi_{Cu} + \varphi_{Al_2O_3}}$,

$C_b = 2k_f + 2(\varphi_{Cu}k_{Cu} + \varphi_{Al_2O_3}k_{Al_2O_3}) - 2(\varphi_{Cu} + \varphi_{Al_2O_3})k_f$, and

$C_c = 2k_f - (\varphi_{Cu}k_{Cu} + \varphi_{Al_2O_3}k_{Al_2O_3}) + (\varphi_{Cu} + \varphi_{Al_2O_3})k_f$.

In like manner;

$$\frac{\rho_{hnf}}{\rho_f} = \varphi_{Cu}\left(\frac{\rho_{Cu}}{\rho_f}\right) + \varphi_{Al_2O_3}\left(\frac{\rho_{Al_2O_3}}{\rho_f}\right) + (1-\varphi_{Cu}-\varphi_{Al_2O_3}), \tag{8}$$

$$\frac{(\rho\beta_T)_{hnf}}{(\rho\beta_T)_f} = \varphi_{Cu}\left(\frac{(\rho\beta_T)_{Cu}}{(\rho\beta_T)_f}\right) + \varphi_{Al_2O_3}\left(\frac{(\rho\beta_T)_{Al_2O_3}}{(\rho\beta_T)_f}\right) + (1-\varphi_{Cu}-\varphi_{Al_2O_3}), \tag{9}$$

$$\frac{(\rho c_p)_{hnf}}{(\rho c_p)_f} = \varphi_{Cu}\left(\frac{(\rho c_p)_{Cu}}{(\rho c_p)_f}\right) + \varphi_{Al_2O_3}\left(\frac{(\rho c_p)_{Al_2O_3}}{(\rho c_p)_f}\right) + (1-\varphi_{Cu}-\varphi_{Al_2O_3}), \tag{10}$$

$$\frac{\sigma_{hnf}}{\sigma_f} = \frac{(D_a + D_b)}{(D_a + D_c)}, \tag{11}$$

where;

$D_a = \frac{(\varphi_{Cu}\sigma_{Cu} + \varphi_{Al_2O_3}\sigma_{Al_2O_3})}{\varphi_{Cu} + \varphi_{Al_2O_3}}$,

$D_b = 2\sigma_f + 2(\varphi_{Cu}\sigma_{Cu} + \varphi_{Al_2O_3}\sigma_{Al_2O_3}) - 2(\varphi_{Al_2O_3} + \varphi_{Cu})\sigma_f$, and

$D_c = 2\sigma_f - (\varphi_{Cu}\sigma_{Cu} + \varphi_{Al_2O_3}\sigma_{Al_2O_3}) + (\varphi_{Cu} + \varphi_{Al_2O_3})\sigma_f$.

Here, φ portrays the nanoparticles volume fraction. Particularly, φ_{Cu} represents the solid copper nanoparticles, $\varphi_{Al_2O_3}$ represents the alumina nanoparticles, and $\varphi_{Cu} + \varphi_{Al_2O_3} = \varphi = 0$ represents the based (water) fluid. In all the computations, we have represented the nanoparticles φ_{Cu} and $\varphi_{Al_2O_3}$ by φ_1 and φ_2, respectively. Moreover, ρ_f, μ_f, $(\rho c_p)_f$, k_f, $(\rho\beta_T)_f$ and σ_f denotes the density, absolute viscosity, TCN, specific heat capacitance, TEC, and electrical conductivity of the based (water) fluid, respectively. Also, the physical data of the carrier-regular fluid and the binary nanoparticles are shown in Table 1. The numerical calculations for this analysis will benefit from these thermophysical features.

Table 1. The thermophysical properties of the hybrid nanofluid.

Properties	$\rho(kg/m^3)$	$c_p(J/\ kgK)$	$\beta_T \times 10^{-5}(1/K)\sigma\ (S/m)$	$k\ (W/mk)$	Pr
Water	997.1	4179	21	5.5×10^{-6}	0.613	6.2
Alumina	3970	765	0.85	35×10^{6}	40	
Copper	8933	385	1.67	59.6×10^{6}	400	—

Moreover, the final term Q^{ccc} in the RHS of Equation (4) demonstrates the part of irregular heat source/sink, which can be established as [43]:

$$Q^{ccc} = \frac{k_{hnf} u_w(x_s)}{x_s v_{hnf}} \left[A_s (T_w - T_\infty) e^{-\xi} + B_s (T_s - T_\infty) \right] \tag{12}$$

Here, A_s denotes the exponential decay space coefficients, and B_s denotes the temperature-dependent heat sink/source. Besides, the situation of a heat absorption or source refers to the positive value of A_s and B_s, whereas the behavior of a heat generation or sink corresponds to the negative value of A_s and B_s. In addition, the second last term q_r in the RHS of Equation (4), called the radiative heat flux, is mathematically demarcated via the Rosseland approximation as [32]:

$$q_r = -\frac{4\sigma^c}{3k^c} \left(\frac{\partial T_s^4}{\partial y_s} \right), \tag{13}$$

where the letter σ^c indicates the Stefan Boltzmann constant and the letter k^c denotes the mean absorption coefficient. By exercising the Taylor series, the fourth power of T_s^4 expanded around a unique point T_∞ and ignoring the higher-order power, one obtains the form as:

$$T_s^4 \cong 4T_s T_\infty^3 - 3T_\infty^4. \tag{14}$$

Hence, by substituting Equations (12)–(14) into Equation (4), the following equation is obtained:

$$\begin{aligned} u_s \frac{\partial T_s}{\partial x_s} + v_s \frac{\partial T_s}{\partial y_s} = \frac{k_{hnf}}{(\rho c_p)_{hnf}} \frac{\partial^2 T_s}{\partial y_s^2} + \frac{16\sigma^c T_\infty^3}{3k^c (\rho c_p)_{hnf}} \frac{\partial^2 T_s}{\partial y_s^2} + \frac{1}{(\rho c_p)_{hnf}} \frac{k_{hnf} u_w(x_s)}{x_s v_{hnf}} \\ \left[A_s (T_w - T_\infty) e^{-\xi} + B_s (T_s - T_\infty) \right]. \end{aligned} \tag{15}$$

Equations (2), (3) and (15), along with BCs (5), need to change into similarity forms by executing the following terms

$$u_w(x_s) = a x_s,\ u_{ex}(x_s) = b x_s,\ v_w(x_s) = -\sqrt{b v_f} f_w \text{ and } T_w(x_s) = T_\infty + T_0 x_s. \tag{16}$$

Here, the constants are mentioned by a and b while f_w denotes the mass transpiration parameter, where $f_w > 0$ indicates the suction, $f_w < 0$ indicates the injection, and $f_w = 0$ indicates the impermeable surface of the sheet. Meanwhile, T_0 signifies the uniform reference temperature, with $T_0 > 0$ indicating the assisting flow (heated surface) while $T_0 < 0$ signifies the opposing flow (cooled surface).

To comfort further the scrutiny of the given model, the following similarity letters or variables are given

$$\xi = y_s \sqrt{\frac{b}{v_f}},\ \psi = \sqrt{b v_f} x_s F(\xi),\ N_s = b\sqrt{b/v_f}\, x_s G(\xi), \theta(\xi) = \frac{T_s - T_\infty}{T_w(x_s) - T_\infty}, \tag{17}$$

where v_f represents the carrier-based fluid (kinematic viscosity). Additionally, the elements of the posited velocity in relation to the "stream function" are defined in the following usual way as

$$u_s = \frac{\partial \psi}{\partial y_s},\ v_s = -\frac{\partial \psi}{\partial x_s}, \tag{18}$$

so that the continuity Equation (1) is true. Also, the components of velocity after utilizing Equation (18) are sealed in the following form:

$$u_s = u_{ex}(x_s)F'(\xi)\,,\ v_s = -\sqrt{bv_f}F(\xi). \tag{19}$$

Putting Equation (17) into governed Equations (2), (3) and (15), we get the following requisite posited ODEs:

$$\frac{\mu_c}{\rho_c}\left(1+\frac{K_c}{\mu_c}\right)F''' - F'^2 + FF'' + 1 + \frac{K_c}{\rho_c}G' + \frac{\sigma_c}{\rho_c}M_c(1-F') + \gamma_c\frac{(\rho\beta_T)_c}{\rho_c}\theta = 0, \tag{20}$$

$$\frac{\mu_c}{\rho_c}\left(1+\frac{K_c}{2\mu_c}\right)G'' + FG' - GF' - \frac{K_c}{\rho_c}E_c(2G+F'') = 0, \tag{21}$$

$$\left(k_c + \frac{4}{3}N_r\right)\theta'' + \Pr(\rho c_p)_c(F\theta' - F'\theta) + \frac{k_c\rho_c}{\mu_c}\left(A_s e^{-\xi} + B_s\theta\right) = 0, \tag{22}$$

where the primes denote the derivative w.r.t to ξ (the pseudo-similarity variable). Let

$$\rho_c = \frac{\rho_{hnf}}{\rho_f}, \mu_c = \frac{\mu_{hnf}}{\mu_f},\ (\rho c_p)_c = \frac{(\rho c_p)_{hnf}}{(\rho c_p)_f}, (\rho\beta_T)_c = \frac{(\rho\beta_T)_{hnf}}{(\rho\beta_T)_f}, k_c = \frac{k_{hnf}}{k_f}, \sigma_c = \frac{\sigma_{hnf}}{\sigma_f}.$$

In Equations (20)–(22), $K_c = \kappa_s/\mu_f$ indicates the material parameter, $E_c = v_f/j_s b$ indicates the micro-inertia factor, $M_c = \sigma_f B_0^2/\rho_f b$ indicates the magnetic factor, $N_r = 4\sigma^c T_\infty^3/k_f k^c$ indicates the radiation factor, and $\gamma_c = \frac{g(\beta_T)_f T_0}{b^2} = Gr_{x_s}/\mathrm{Re}_{x_s}^2$ indicates the buoyancy or mixed convective factor, where $\mathrm{Re}_{x_s} = x_s u_{ex}/v_f$ and $Gr_{x_s} = g\beta_T(T_w - T_\infty)x_s^3/{v_f}^2$ identify as the local Reynolds number and the local Grashof number, respectively. The BCs (5) can be rewritten in the dimensionless form and are

$$\begin{aligned} &F'(0) = \varepsilon_c = \tfrac{a}{b},\ F(0) = f_w,\ G(0) = -m_s F''(0),\ \theta(0) = 1,\\ &F'(\xi)\to 1,\ G(\xi)\to 0,\ \ \theta(\xi)\to 0,\ \ \text{at } \xi\to\infty. \end{aligned} \tag{23}$$

In Equation (23), ε_c is the stretched or contracted parameter where $\varepsilon_c > 0$ is for stretching, $\varepsilon_c < 0$ is for shrinking, and $\varepsilon_c = 0$ is for static.

2.1. The Engineering Quantities of Interest

The behaviors of the thermo-micropolar HN flow in the current model are described using the surface shear stress, gradient of microrotation, and rate of heat transfer.

2.1.1. The Shear Stress Coefficient (SSC)

The SSC is demarcated as

$$C_f = \frac{\tau_w}{\rho_f u_{ex}^2}\,, \tag{24}$$

where $\tau_w = \left(\left(\mu_{hnf} + \kappa_s\right)\frac{\partial u_s}{\partial y_s} + \kappa_s N_s\right)\Big|_{y_s=0}$ is the wall SS for the micropolar HN. Substituting Equation (17) into Equation (24), the reduced SSC may be expressed as

$$\mathrm{Re}_{x_s}^{1/2}C_f = (\mu_c + K_c(1-m_s))F''(0). \tag{25}$$

2.1.2. The Couple-Stress Coefficient (CSC)

The CSC is demarcated as

$$C_g = \frac{M_w v_f}{\rho_f j_s u_{ex}^3}. \tag{26}$$

Here, the wall CS of the micropolar HN is signified by $M_w = \gamma_{hnf} \frac{\partial N_s}{\partial y_s}\Big|_{y_s=0}$, in which $\gamma_{hnf} = \left(\frac{2\mu_{hnf} + \kappa_s}{2}\right) j_s$ corresponds to the spin gradient of the HN. The following dimensionless form of the CSC is obtained by using Equation (17) in the aforementioned equation.

$$\mathrm{Re}_{x_s} C_g = \left(\mu_c + \frac{K_c}{2}\right) G'(0). \tag{27}$$

2.1.3. The Heat Transfer Rate (HTR)

The HTR at the surface is demarcated as

$$Nu_{x_s} = \frac{x_s q_w}{k_f (T_w(x_s) - T_\infty)}, \tag{28}$$

where $q_w = \left(-k_{hnf} \frac{\partial T_s}{\partial y_s} + q_r\right)\Big|_{y_s=0}$ specifies the heat flux at the wall surface for the micropolar HN. Finally, using the similarity variables in Equation (28), one obtains the following dimensionless form of the HTR

$$\mathrm{Re}_{x_s}^{-1/2} Nu_{x_s} = -\left(k_c + \frac{4}{3} N_r\right) \theta'(0). \tag{29}$$

3. Stability Analysis

The problem of hybrid nanofluids has been numerically addressed and admits two dissimilar (FBS and SBS) solutions. As a result, Merkin [44] and Weidman et al. [45] have documented the dual branch results for issues with a different geometry, where the FBS is stable and physically compatible while the SBS is unreliable and not generally appropriate. In light of these published works, we must put the two-point problem of the governing Equations (2)–(4) in the unsteady form while leaving Equation (1) unchanged to examine the characteristics. The following are the time-dependent equations:

$$\begin{aligned} &\frac{\partial u_s}{\partial t_s} + u_s \frac{\partial u_s}{\partial x_s} + v_s \frac{\partial u_s}{\partial y_s} = u_{ex} \frac{du_{ex}}{dx_s} + \frac{(\mu_{hnf} + \kappa_s)}{\rho_{hnf}} \frac{\partial^2 u_s}{\partial y_s^2} + \frac{\sigma_{hnf} B_0^2}{\rho_{hnf}} (u_{ex} - u_s) \\ &+ \frac{\kappa_s}{\rho_{hnf}} \frac{\partial N_s}{\partial y_s} + \frac{g(\rho\beta_T)_{hnf}}{\rho_{hnf}} (T_s - T_\infty), \end{aligned} \tag{30}$$

$$\frac{\partial N_s}{\partial t_s} + u_s \frac{\partial N_s}{\partial x_s} + v_s \frac{\partial N_s}{\partial y_s} = \frac{\left(\mu_{hnf} + \kappa_s/2\right)}{\rho_{hnf}} \frac{\partial^2 N_s}{\partial y_s^2} - \frac{\kappa_s}{j_s \rho_{hnf}} \left(2N_s + \frac{\partial u_s}{\partial y_s}\right), \tag{31}$$

$$\frac{\partial T_s}{\partial t_s} + u_s \frac{\partial T_s}{\partial x_s} + v_s \frac{\partial T_s}{\partial y_s} = \frac{k_{hnf}}{(\rho c_p)_{hnf}} \frac{\partial^2 T_s}{\partial y_s^2} - \frac{1}{(\rho c_p)_{hnf}} \frac{\partial q_r}{\partial y_s} + \frac{1}{(\rho c_p)_{hnf}} Q^{ccc}, \tag{32}$$

In light of this, we express the new-fangled time variable $\Sigma_c = bt_s$ here. For the analysis of the problem under consideration, we must rephrase the new non-dimensional variables using similarity Variables (17) as follows:

$$\begin{aligned} &\xi = y_s \sqrt{\frac{b}{v_f}},\ u_s = b x_s \frac{\partial F(\xi, \Sigma_c)}{\partial \xi},\ N_s = b \sqrt{b/v_f}\, x_s G(\xi, \Sigma_c), \\ &\theta(\xi, \Sigma_c) = \frac{T_s - T_\infty}{T_w - T_\infty}, v_s = -\sqrt{b v_f}\, F(\xi, \Sigma_c),\ \Sigma_c = bt_s. \end{aligned} \tag{33}$$

Now implementing Equation (33) into Equations (30)–(32) along with BCs (5), we capture the following form:

$$\begin{aligned} &\frac{\mu_c}{\rho_c}\left(1 + \frac{K_c}{\mu_c}\right) \frac{\partial^3 F}{\partial \xi^3} - \left(\frac{\partial F}{\partial \xi}\right)^2 + F \frac{\partial^2 F}{\partial \xi^2} + 1 + \frac{K_c}{\rho_c} \frac{\partial G}{\partial \xi} + \frac{\sigma_c}{\rho_c} M_c \left(1 - \frac{\partial F}{\partial \xi}\right) + \\ &\gamma_c \frac{(\rho\beta_T)_c}{\rho_c} \theta - \frac{\partial^2 F}{\partial \xi \partial \Sigma_c} = 0, \end{aligned} \tag{34}$$

$$\frac{\mu_c}{\rho_c}\left(1+\frac{K_c}{2\mu_c}\right)\frac{\partial^2 G}{\partial \xi^2}+F\frac{\partial G}{\partial \xi}-G\frac{\partial F}{\partial \xi}-\frac{K_c}{\rho_c}E_c\left(2G+\frac{\partial^2 F}{\partial \xi^2}\right)-\frac{\partial G}{\partial \Sigma_c}=0, \tag{35}$$

$$\left(k_c+\frac{4}{3}N_r\right)\frac{\partial^2 \theta}{\partial \xi^2}+\Pr(\rho c_p)_c\left(F\frac{\partial \theta}{\partial \xi}-\theta\frac{\partial F}{\partial \xi}\right)+\frac{k_c\rho_c}{\mu_c}\left(A_s e^{-\xi}+B_s\theta\right)-\frac{\partial \theta}{\partial \Sigma_c}=0, \tag{36}$$

and the distorted BCs become

$$\begin{array}{l}\frac{\partial F(0,\Sigma_c)}{\partial \xi}=\varepsilon_c,\ F(0,\Sigma_c)=f_w,\ G(0,\Sigma_c)=-m_s\frac{\partial^2 F(0,\Sigma_c)}{\partial \xi^2},\ \theta(0,\Sigma_c)=1,\\ \frac{\partial F(\xi,\Sigma_c)}{\partial \xi}\to 1,\ G(\xi,\Sigma_c)\to 0,\ \ \theta(\xi,\Sigma_c)\to 0,\ \ \text{at } \xi\to\infty.\end{array} \tag{37}$$

The steady results are perturbed to test the stability of the outcomes over time $F(\xi)=F_0(\xi)$, $G(\xi)=G_0(\xi)$, and $\theta(\xi)=\theta_0(\xi)$ as (see Merkin [44] and Weidman et al. [45]):

$$\begin{array}{l}F(\xi,\Sigma_c)=F_0(\xi)+e^{-\lambda_a\Sigma_c}f(\xi),\ G(\xi,\Sigma_c)=G_0(\xi)+e^{-\lambda_a\Sigma_c}g(\xi),\\ \theta(\xi,\Sigma_c)=\theta_0(\xi)+e^{-\lambda_a\Sigma_c}h(\xi).\end{array} \tag{38}$$

Here, the notation λ_a is an unknown eigenvalue parameter, and functions $f(\xi)$, $g(\xi)$, and $h(\xi)$ are small relative to $F_0(\xi)$, $G_0(\xi)$, and $\theta_0(\xi)$, respectively. The problem of linearized eigenvalues is given as follows using Equation (38) into Equations (34)–(36) as well as the boundary Conditions (37).

$$\frac{\mu_c}{\rho_c}\left(1+\frac{K_c}{\mu_c}\right)f'''+F_0''f+f''F_0-2f'F_0'+\frac{K_c}{\rho_c}g'-\frac{\sigma_c}{\rho_c}M_c f'+\gamma_c\frac{(\rho\beta_T)_c}{\rho_c}h+\lambda_a f'=0, \tag{39}$$

$$\frac{\mu_c}{\rho_c}\left(1+\frac{K_c}{2\mu_c}\right)g''+fG_0'+F_0g'-G_0f'-F_0'g-\frac{K_c}{\rho_c}E_c(2g+f'')+\lambda_a g=0, \tag{40}$$

$$\left(k_c+\frac{4}{3}N_r\right)h''+\Pr(\rho c_p)_c\left(F_0h'+f\theta_0'-\theta_0f'-hF_0'\right)+\left(\frac{k_c\rho_c}{\mu_c}B_s+\lambda_a\right)h=0, \tag{41}$$

and the altered BCs become

$$\begin{array}{l}f'(0)=0,\ \ f(0)=0,\ \ g(0)=-m_s f''(0),\ \ h(0)=0,\\ f'(\xi)\to 0,\ \ g(\xi)\to 0,\ \ \ h(\xi)\to 0,\ \ \ at\ \xi\to\infty.\end{array} \tag{42}$$

The values of λ_a in Equations (39)–(41) are attained by setting the default value of $f''(0)$, $g'(0)$, or $h'(0)$. Lastly, the system of Equations (39)–(42) can be solved by setting $f''(0)=1$ to get the minimum eigenvalues λ_a, see (Harris et al. [46]).

4. Multiple Solution Methodology and Authentication of the Code

This portion of the paper demonstrates the problem-solving approaches together with the consequences of the numerical/computational procedure as well as the accuracy or confirmation/validation of the scheme. The associated non-linear ODE Equations (20)–(22) along with the boundary conditions (BCs) mentioned in Equation (23) were calculated from the essential/main system of governing equations by utilizing the similarity variables/transformations. These systems of equations are extremely complicated and nonlinear, and it is challenging to find their solutions through exact/analytical methods. Hence, bvp4c uses numerical computation/simulation to compute these acquired non-linear similarity equations. The three-stage Lobatto IIIA formulation is further achieved using a "built-in" type in the MATLAB program that workouts the well-known finite-difference method. References [47–49] provide more details on the approach under consideration. Using the new (notations) variables, the higher second-order and third-order ODEs were transformed into the first-order respective similarity equations. For ongoing existing techniques of the system, the variables are chosen as under:

$$F=\Sigma_1,\ F'=\Sigma_2, F''=\Sigma_3, G=\Sigma_4, G'=\Sigma_5, \theta=\Sigma_6, \theta'=\Sigma_7, \tag{43}$$

By exercising the new notations/variables in the transformed system of Equations (20)–(22), the following set of first-order ODEs can take place:

$$\frac{d}{d\xi}\begin{pmatrix}\Sigma_1\\ \Sigma_2\\ \Sigma_3\\ \Sigma_4\\ \Sigma_5\\ \Sigma_6\\ \Sigma_7\end{pmatrix}=\begin{pmatrix}\Sigma_2\\ \Sigma_3\\ \frac{\rho_c}{\mu_c\left(1+\frac{K_c}{\mu_c}\right)}\left({\Sigma_2}^2-1-\Sigma_1\Sigma_3-\frac{K_c}{\rho_c}\Sigma_5-\frac{\sigma_c}{\rho_c}M_c(1-\Sigma_2)-\frac{(\rho\beta_T)_c}{\rho_c}\gamma_c\Sigma_6\right)\\ \Sigma_5\\ \frac{\rho_c}{\mu_c\left(1+\frac{K_c}{2\mu_c}\right)}\left(\Sigma_2\Sigma_4-\Sigma_1\Sigma_5+\frac{K_c}{\rho_c}E_c(2\Sigma_4+\Sigma_3)\right)\\ \Sigma_7\\ \frac{1}{(k_c+(4/3)N_r)}\left(\mathrm{Pr}(\rho c_p)_c(\Sigma_2\Sigma_6-\Sigma_1\Sigma_7)-\frac{k_c\rho_c}{\mu_c}\left(A_se^{-\xi}+B_s\Sigma_6\right)\right)\end{pmatrix}, \quad (44)$$

with the transformed boundary conditions:

$$\begin{cases}\Sigma_1(0)=f_w,\Sigma_2(0)=\varepsilon_c,\Sigma_4(0)=-m_s\Sigma_3(0),\Sigma_6(0)=1,\\ \Sigma_2(\infty)\to 1,\Sigma_4(\infty)\to 0,\Sigma_6(\infty)\to 0.\end{cases}. \quad (45)$$

During this working process, the system needed early predictions whose outputs satisfied the set of first-order ODE (44) as well as the pertinent BCs (45). The problem has been resolved for the two distinct branches of the solution. As a result, the system needs two separate initial assumptions. The first guess for the first branch solution is quite evident; however, choosing the right guess for the second branch solution that asymptotically meets the boundary requirements involves more work. Furthermore, a suitable default value of $\xi\to\infty$ was selected, such as the thickness of the required boundary layer, $\xi=\xi_\infty=5.0$, with the relative tolerance/marginal error set up to 10^{-6}. In order to verify the numerical outcomes obtained for the first and second branches, we have compared our shear stress coefficient and couple-stress coefficient results with those reported by Lok et al. [50], which have been presented in Tables 2 and 3. Additionally, it was revealed that the current outcomes were in exceptional agreement, indicating that the computational code used in this examination was flawless/perfect. Thus, the outcomes were taken to be accurate and consistent or reliable.

Table 2. Values of shear stress for the several values of γ_c and K_c when $\varepsilon_c=0$, $f_w=0$, $\varphi_1=0$, $\varphi_2=0$, $E_c=1$, $M_c=0$, $m_s=0$, and $\mathrm{Pr}=0.7$.

γ_c	K_c	Lok et al. [50]		Present Solution	
		FBS	**SBS**	**FBS**	**SBS**
−1.1	0.0	0.631500	−0.350112	0.631412	−0.350102
−1.4	-	0.440161	−0.494103	0.440116	−0.494124
−1.7	-	0.225110	−0.574153	0.225075	−0.574135
−2.0	-	−0.039513	−0.578523	−0.039541	−0.578493
−1.1	3.0	0.338030	-	0.337967	-
−1.4	-	0.272370	−0.232634	0.272212	−0.232728
−1.7	-	0.202475	−0.273943	0.202345	−0.273934
−2.0	-	0.126644	−0.030171	0.126452	−0.030198

Table 3. Values of couple-stress coefficient for the several values of γ_c and K_c when $\varepsilon_c = 0$, $f_w = 0$, $\varphi_1 = 0$, $\varphi_2 = 0$, $E_c = 1$, $M_c = 0$, $m_s = 0$, and Pr = 0.7.

γ_c	K_c	Lok et al. [50]		Present Solution	
		FBS	**SBS**	**FBS**	**SBS**
−1.1	0.0	0.623635	−0.174194	0.623650	−0.174172
−1.4	-	0.590886	−0.044680	0.590846	−0.044371
−1.7	-	0.549045	0.073812	0.590150	0.073804
−2.0	-	0.486596	0.198590	0.486586	0.198590
−1.1	3.0	0.541705	-	0.541039	-
−1.4	-	0.523084	−0.149594	0.523015	−0.149688
−1.7	-	0.502440	−0.059305	0.502333	−0.059348
−2.0	-	0.477867	0.020600	0.477732	0.020533

5. Analysis of Results

The thermo-micropolar (water/Cu-Al_2O_3) hybrid nanofluid and heat transfer flow examination comprised several distinct distinguished parameters which are namely and symbolically denoted as M_c for the magnetic factor, K_c for the material factor, E_c for the micro-inertia factor, N_r for the radiation factor, f_w for the mass suction/injection factor, ε_c for the stretched/shrinked factor, γ_c for the mixed convection or buoyancy factor, and φ_1 and φ_2 for the solid nanoparticles volume fraction. The physical impact of these numerous notable influential parameters on the shear stress coefficient, couple-stress coefficient, heat transfer, and temperature profile was presented tabularly in Tables 4–6, but graphically illustrated in Figures 2–16, respectively. However, the eigenvalue λ_a for the several/sundry values of ε_c is established in Figure 17 while the streamlines are presented in Figures 18 and 19. For the computation purpose, we have executed the following ranges for the parameters such as $-5.0 < \varepsilon_c < 5.0$, $-15.0 < \gamma_c < 15.0$, $-3.0 < f_w < 3.0$, $0.0 < M_c < 1.0$, $0.0 < E_c < 1.0$, $m_s = 0.5$, $0.0 < N_r < 5.0$, $-1.0 < A_s < 1.0$, $0.0 < K_c < 1.0$, and $-1.0 < B_s < 1.0$. Furthermore, the first branch solution (FBS) and second branch solution (SBS) are highlighted by the complete filled solid and dashed black lines, respectively, while the black solid balls denoted the critical or bifurcation points.

Table 4. Quantitative values of SSC for the several distinct parameters when $\varepsilon_c = -1.5$, $\gamma_c = -1.0$, $E_c = 0.5$, $m_s = 0.5$, $N_r = 2.0$, $A_s = 0.1$ and $B_s = 0.1$.

φ_1, φ_2	K_c	M_c	f_w	**FBS**	**SBS**
0.025	0.25	0.20	1.0	3.2811	1.2167
0.030	-	-	-	3.4592	1.2056
0.035	-	-	-	3.6352	1.1979
0.025	0.25	0.20	1.0	3.2811	1.2167
-	0.30	-	-	3.2775	1.2558
-	0.35	-	-	3.2733	1.2952
0.025	0.25	0.20	1.0	3.2811	1.2167
-	-	0.25	-	3.4014	1.1981
-	-	0.30	-	3.5140	1.1882
0.025	0.25	0.20	0.90	2.8005	1.4393
-	-	-	0.95	3.0547	1.3151
-	-	-	1.0	3.2811	1.2167

Table 5. Quantitative values of CSC for the several distinct parameters when $\varepsilon_c = -1.5$, $\gamma_c = -1.0$, $f_w = 1.0$, $M_c = 0.20$, $m_s = 0.5$, $N_r = 2.0$, $A_s = 0.1$, and $B_s = 0.1$.

φ_1, φ_2	K_c	E_c	FBS	SBS
0.025	0.25	0.5	0.8057	−0.3938
0.030	-	-	0.8956	−0.4363
0.035	-	-	0.9843	−0.4786
0.025	0.25	0.5	0.8057	−0.3938
-	0.30	-	0.7696	−0.3929
-	0.35	-	0.7344	−0.3909
0.025	0.25	0.1	0.8144	−0.3519
-	-	0.3	0.8099	−0.3745
-	-	0.5	0.8057	−0.3938

Table 6. Quantitative values of the HTR for the several distinct parameters when $\varepsilon_c = -1.5$, $\gamma_c = -1.0$, $f_w = 1.0$, $M_c = 0.20$, $E_c = 0.5$, $m_s = 0.5$, $N_r = 2.0$, $A_s = 0.1$, and $B_s = 0.1$.

φ_1, φ_2	N_r	A_s, B_s	FBS	SBS
0.025	2.0	0.1	2.1035	−6.8374
0.030	-	-	2.2358	−7.3791
0.035	-	-	2.3492	−7.9004
0.025	1.5	0.1	2.0141	−7.1554
-	2.0	-	2.1035	−6.8374
-	2.5	-	2.2270	−6.5757
0.025	2.0	0.1	2.1035	−6.8374
-	-	0.2	1.8660	−6.9680
-	-	0.3	1.6205	−7.0865
	-	−0.1	2.5575	−6.5426
	-	−0.2	2.7750	−6.3797
	-	−0.3	2.9868	−6.2073

Tables 4 and 5 demonstrate the quantitative values of the shear stress coefficient (SSC) and couple-stress coefficient (CSC) for the FBS as well as the SBS due to the distinct values of the solid nanoparticles' volume fraction, material parameter, magnetic parameter, mass suction parameter, and the micro-inertia parameter, respectively, when $\varepsilon_c = -1.5$, $\gamma_c = -1.0$, $m_s = 0.5$, $N_r = 2.0$, $A_s = 0.1$, and $B_s = 0.1$. It was observed that the shear stress coefficient for the FBS escalated and decelerated for the SBS with the superior impact of M_c, f_w, φ_1, and φ_2 while contrary behavior was seen in two outcome branches for the larger values of K_c (see Table 4). Generally, the higher magnetic impression creates the strong Lorentz force by which the velocity profile declines. As a result, the speed/motion of the fluid (or velocity profile) has an inverse relation with the skin friction coefficient. According to the basic rule of physics, if the velocity of the fluid shrinks with strong influences of the magnetic parameter, as a response the shear stress coefficient uplifts. On the other hand, the output values pattern/tendency of the CSC for the FBS remains the same as (the SSC) with the larger impacts of φ_1 and φ_2 while it declines for the SBS, and also magnitude-wise, is augmented. Furthermore, the CSC diminished for both FB and SB outcomes with augmentation in the values of K_c and E_c as depicted in Table 5. Generally, the absolute/dynamic viscosity of the fluid reduces due to the higher influences of the material parameter, hence, the CSC lessens.

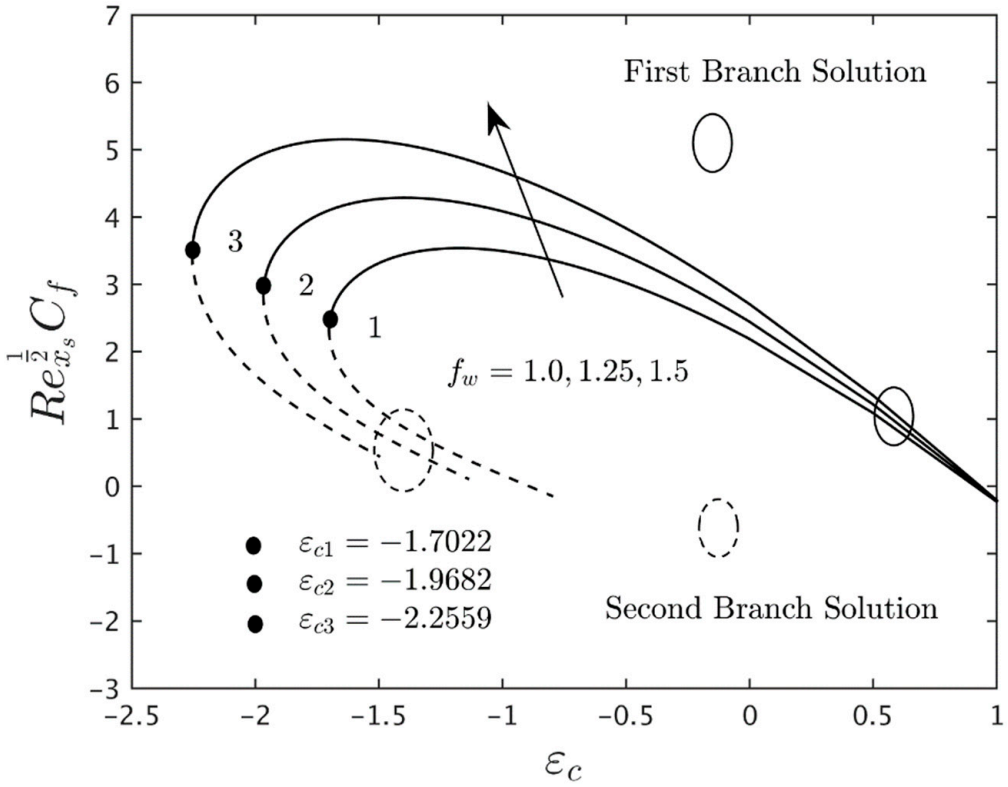

Figure 2. Variation of the skin friction coefficient with ε_c for the several values of the f_w.

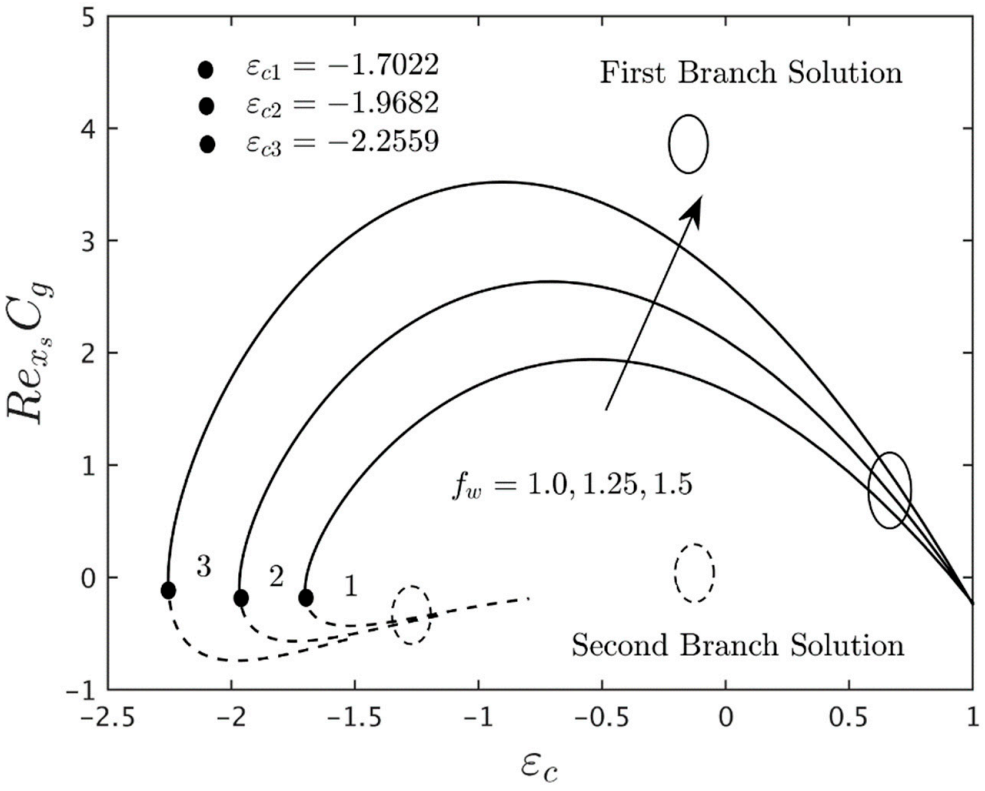

Figure 3. Variation of the couple stress coefficient with ε_c for the several values of f_w.

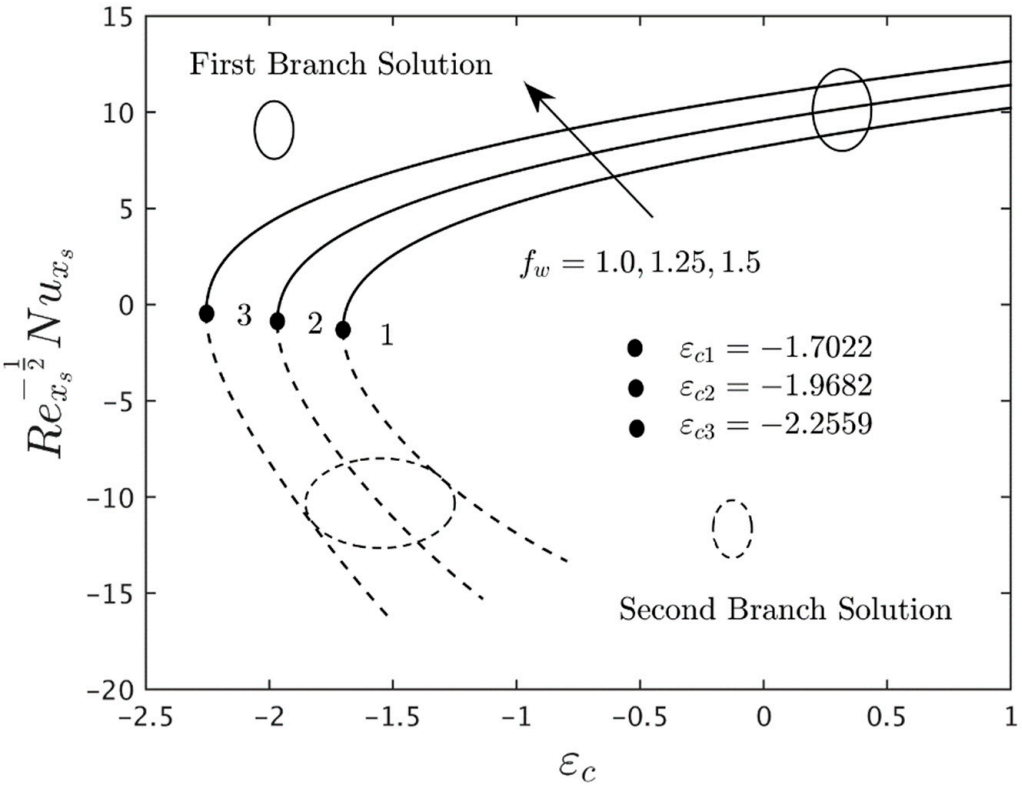

Figure 4. Variation of the heat transfer with ε_c for the several values of f_w.

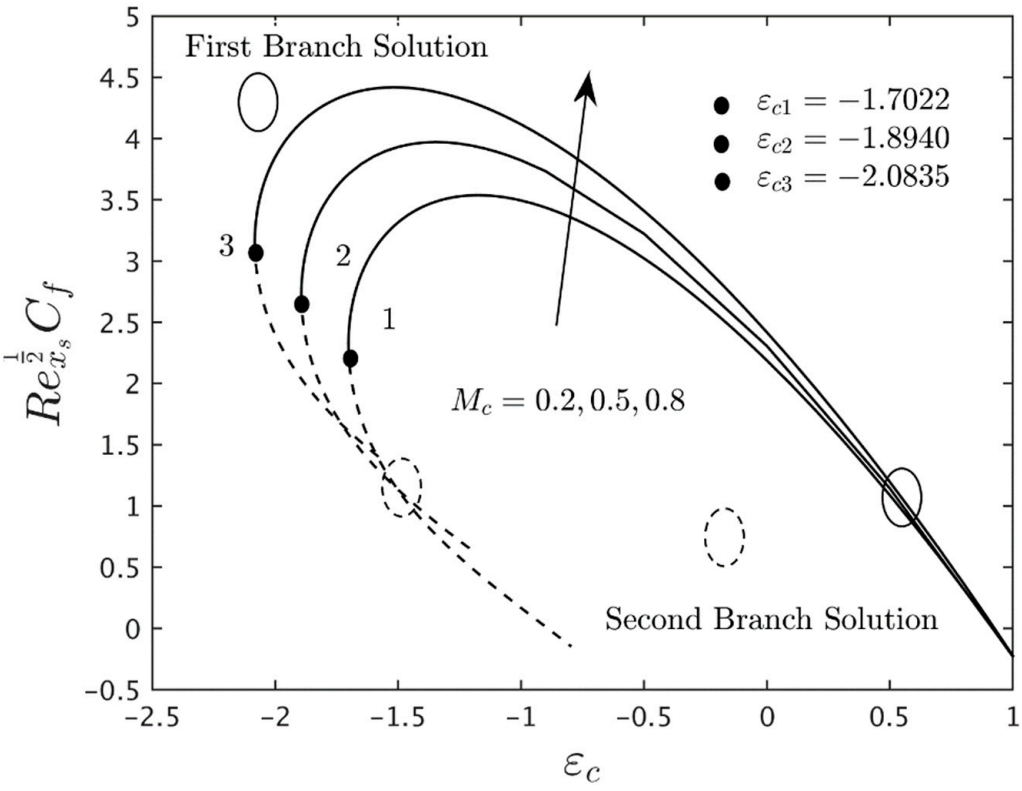

Figure 5. Variation of the SSC with ε_c for the several values of M_c.

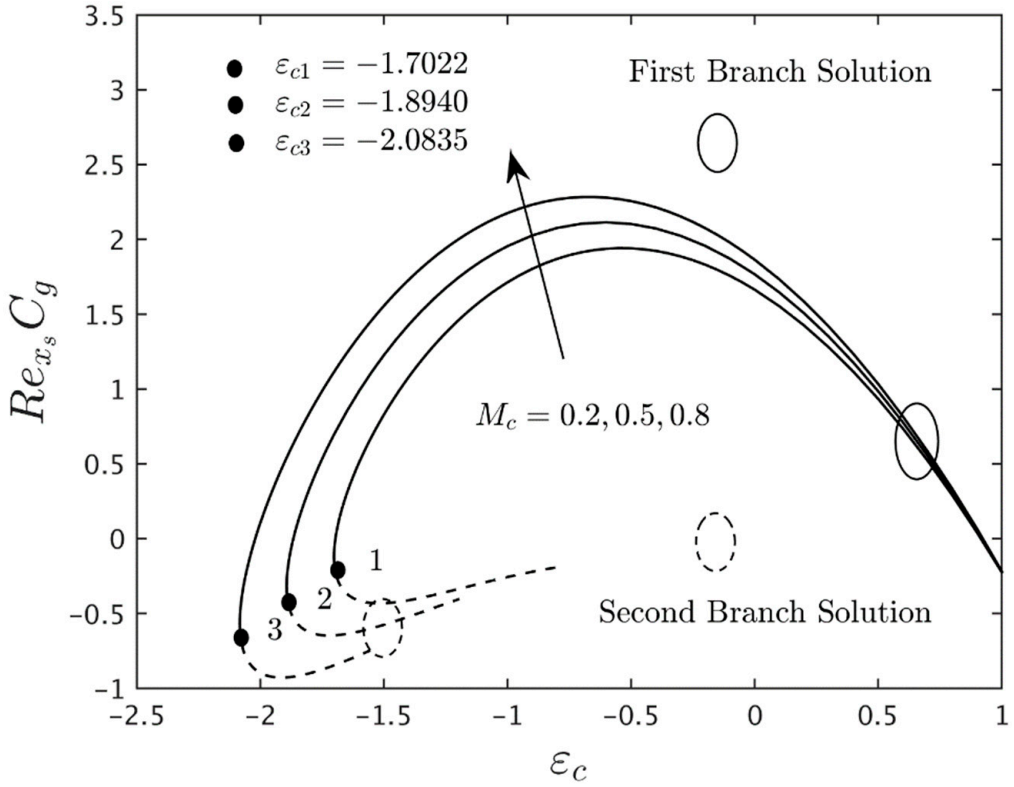

Figure 6. Variation of the CSC with ε_c for the several values of M_c.

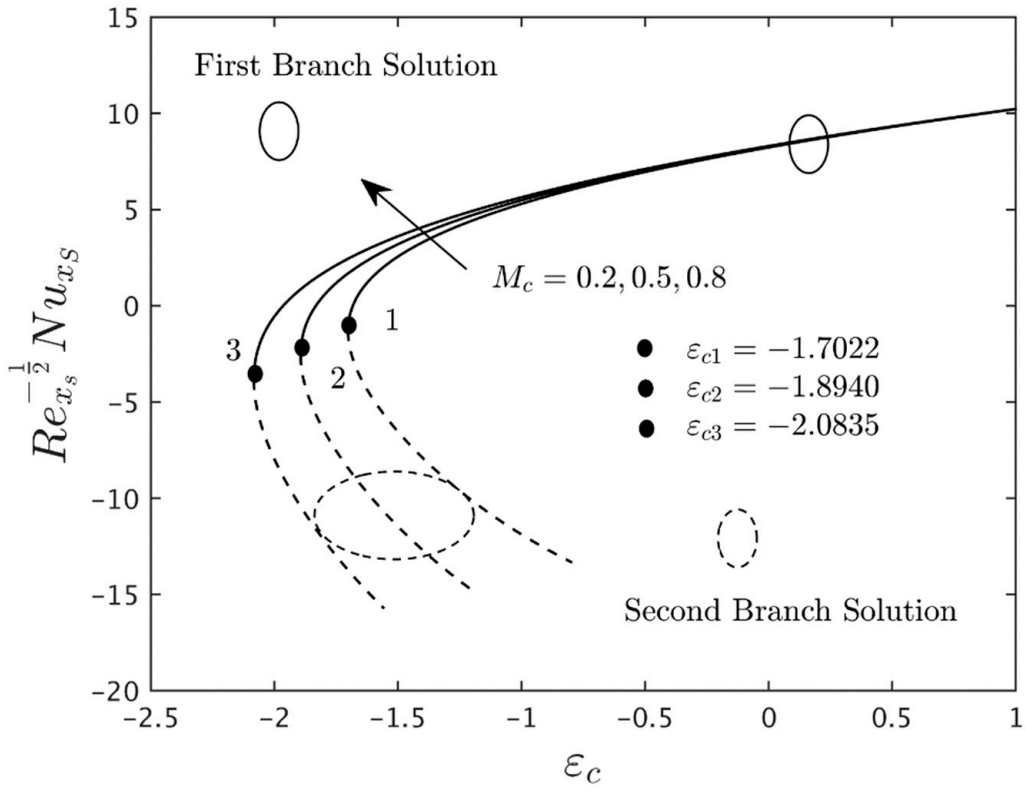

Figure 7. Variation of the HTR with ε_c for the several values of M_c.

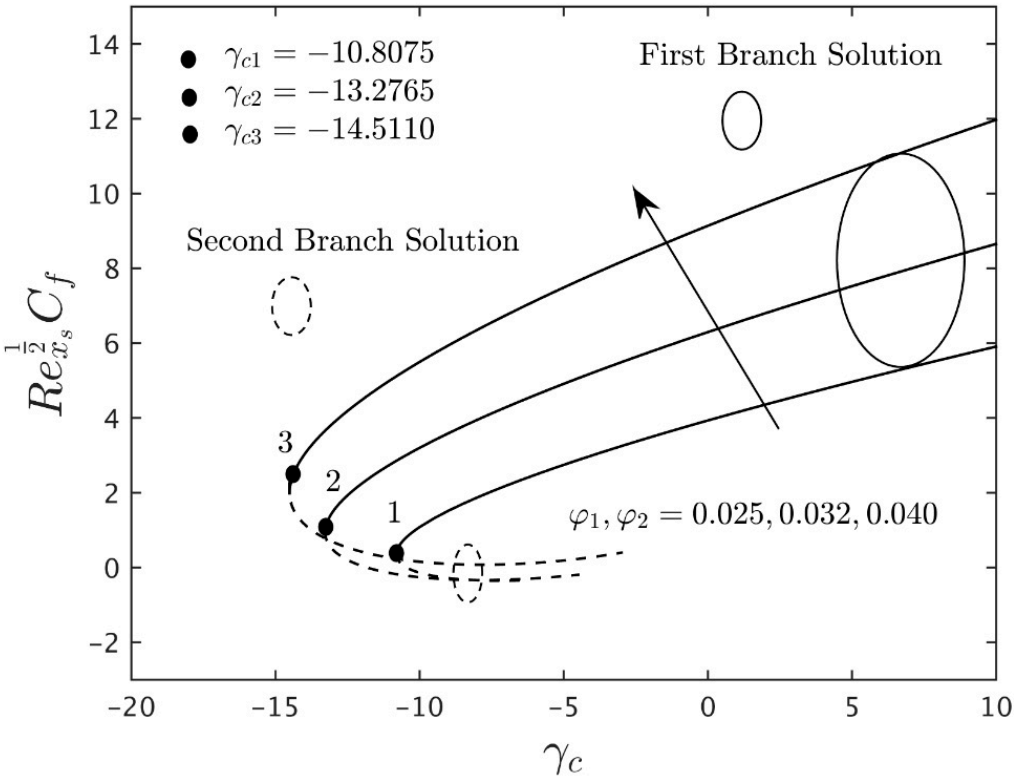

Figure 8. Variation of the skin friction coefficient with γ_c for the several values of φ_1 and φ_2.

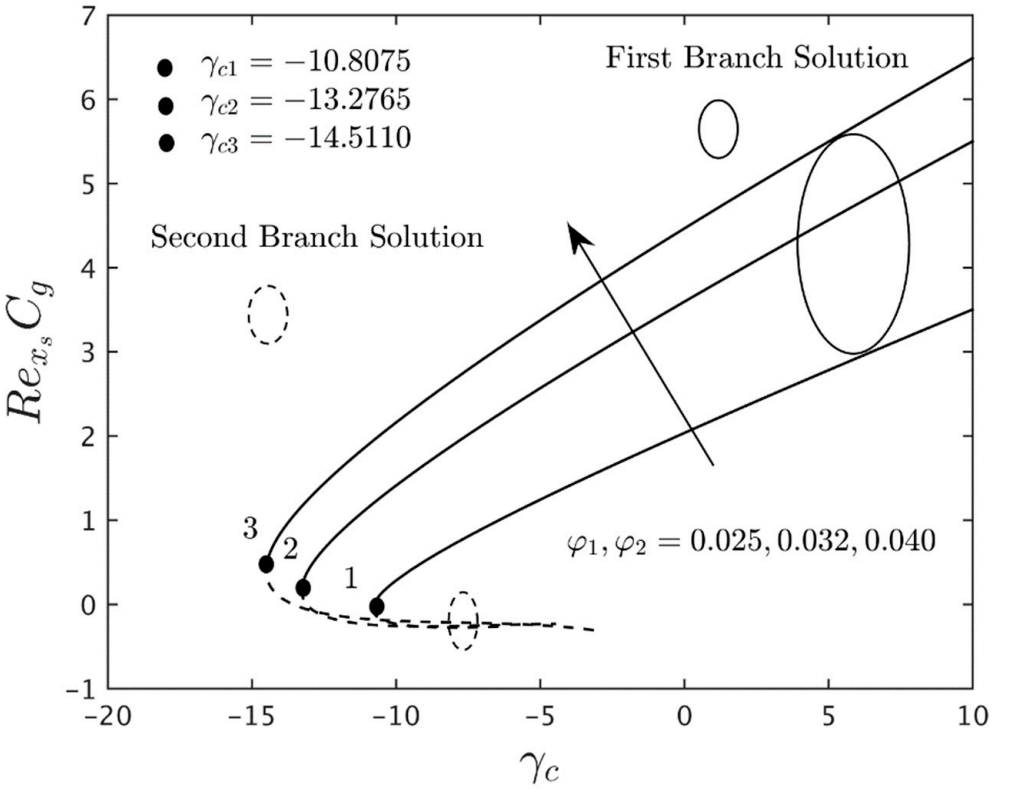

Figure 9. Variation of the couple stress coefficient with γ_c for the several values of φ_1 and φ_2.

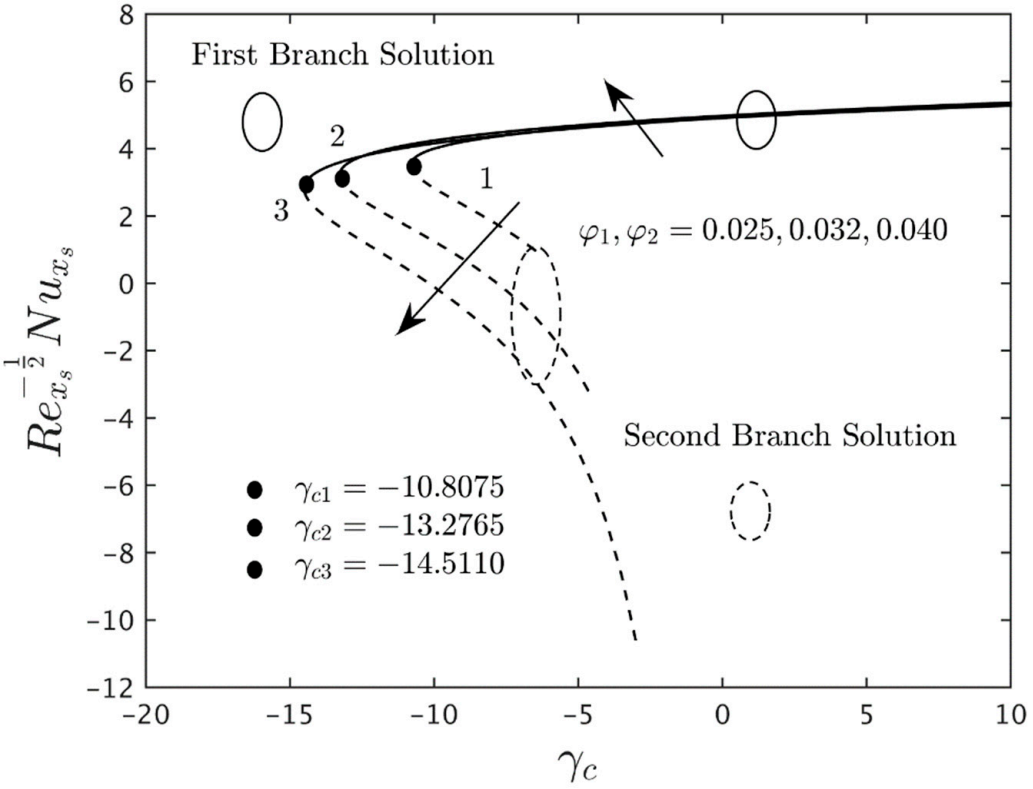

Figure 10. Variation of the heat transfer with γ_c for the several values of φ_1 and φ_2.

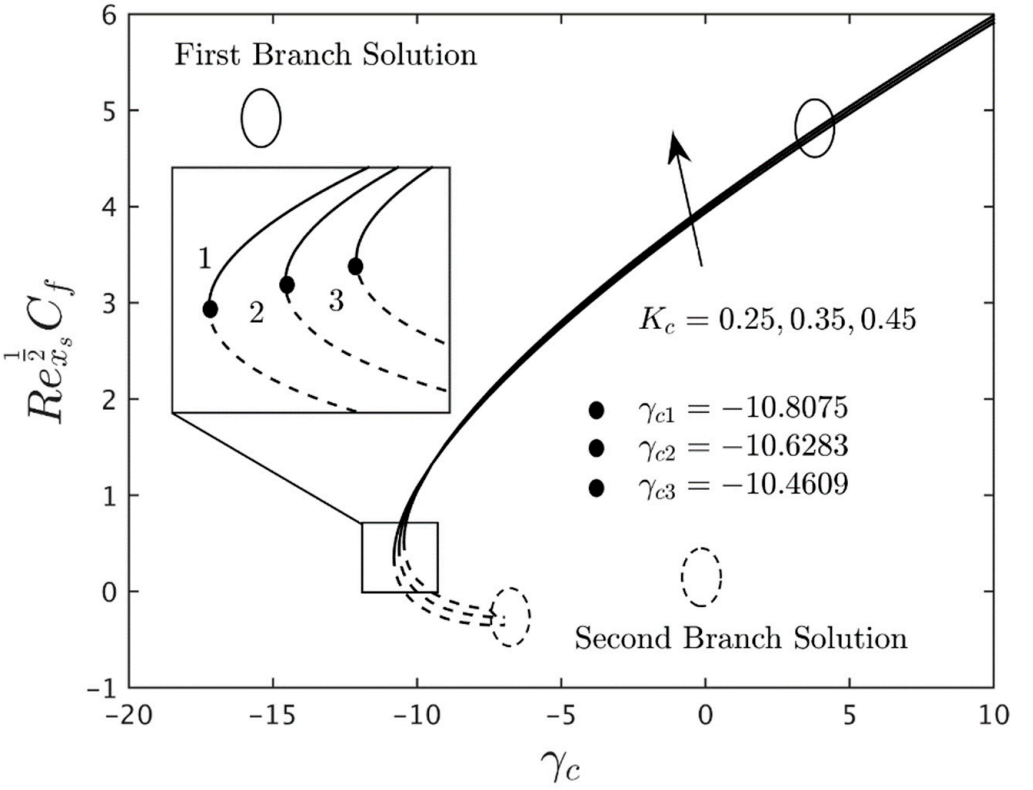

Figure 11. Variation of the skin friction coefficient with γ_c for the several values of K_c.

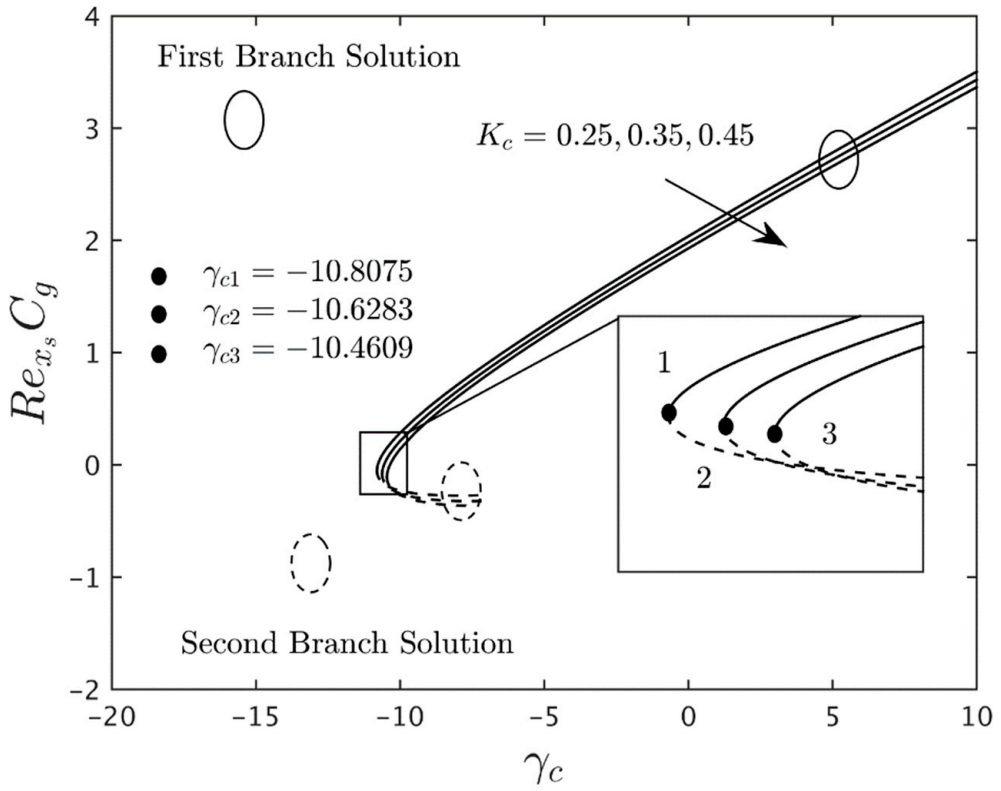

Figure 12. Variation of the couple stress coefficient with γ_c for the several values of K_c.

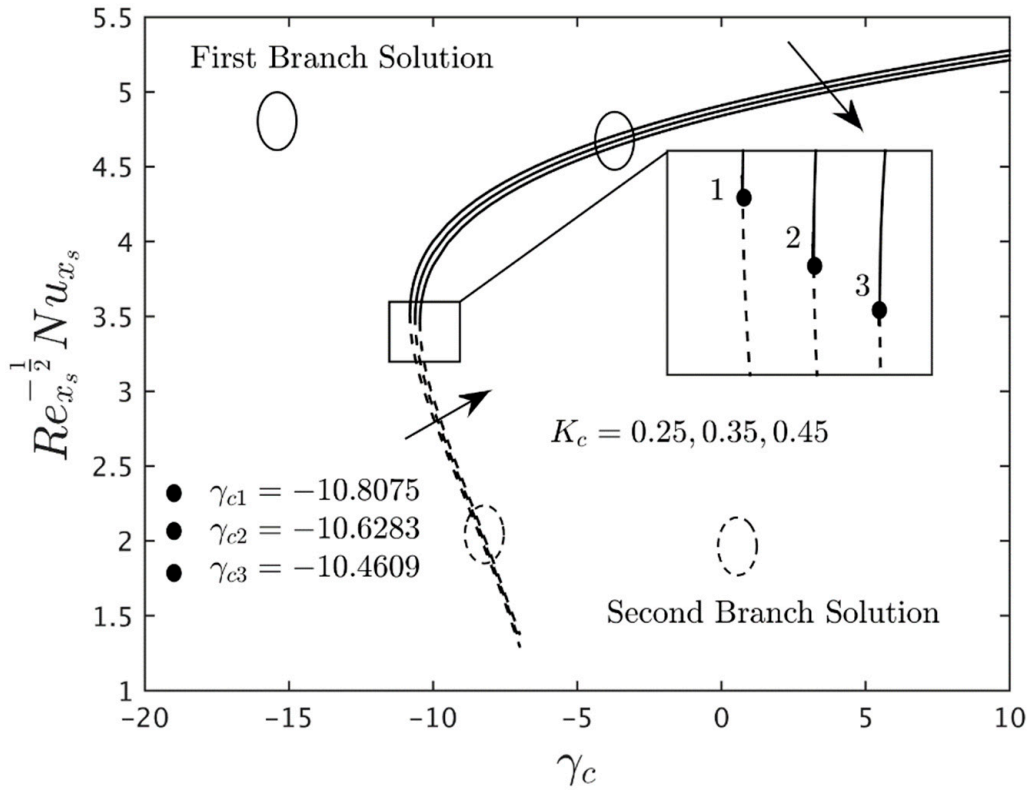

Figure 13. Variation of the heat transfer with γ_c for the several values of K_c.

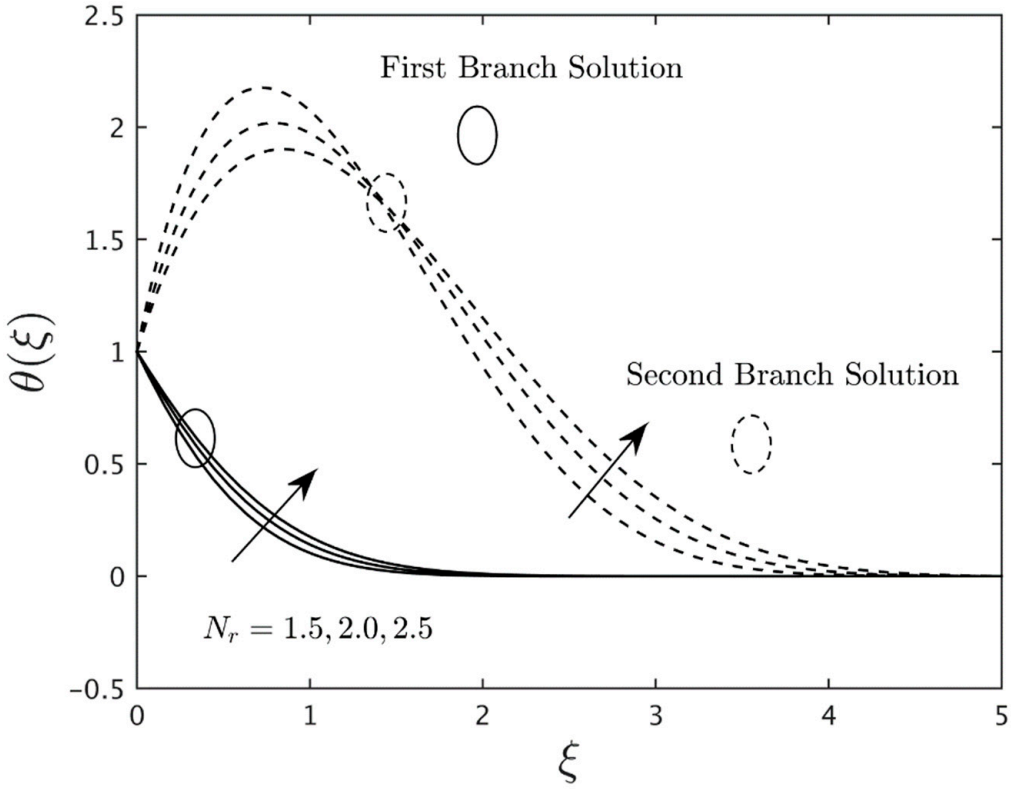

Figure 14. Temperature profile for the several values of N_r.

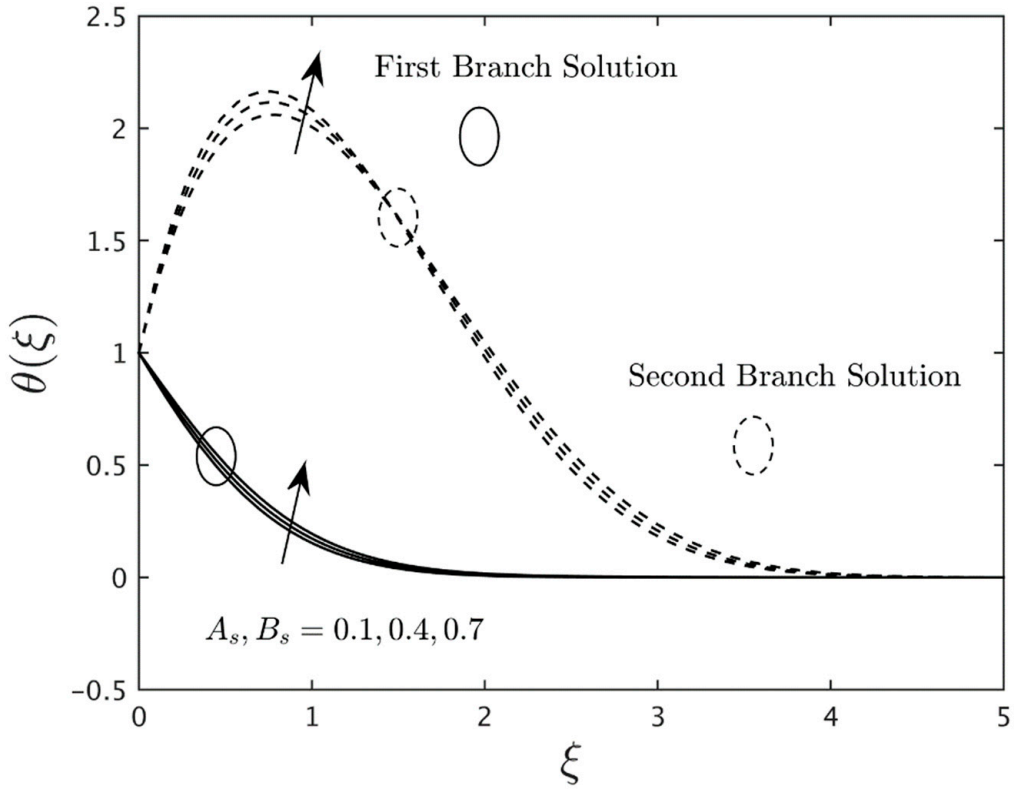

Figure 15. Temperature profile for the several values of $A_s, B_s > 0$.

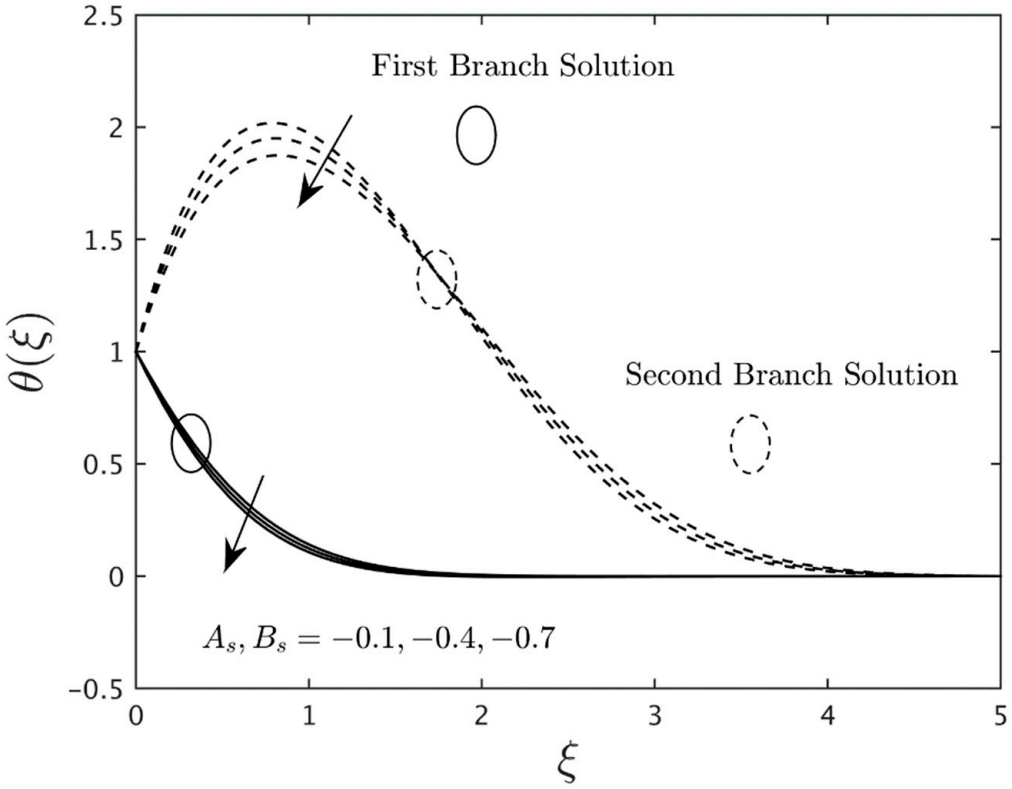

Figure 16. Temperature profile for the several values of $A_s, B_s < 0$.

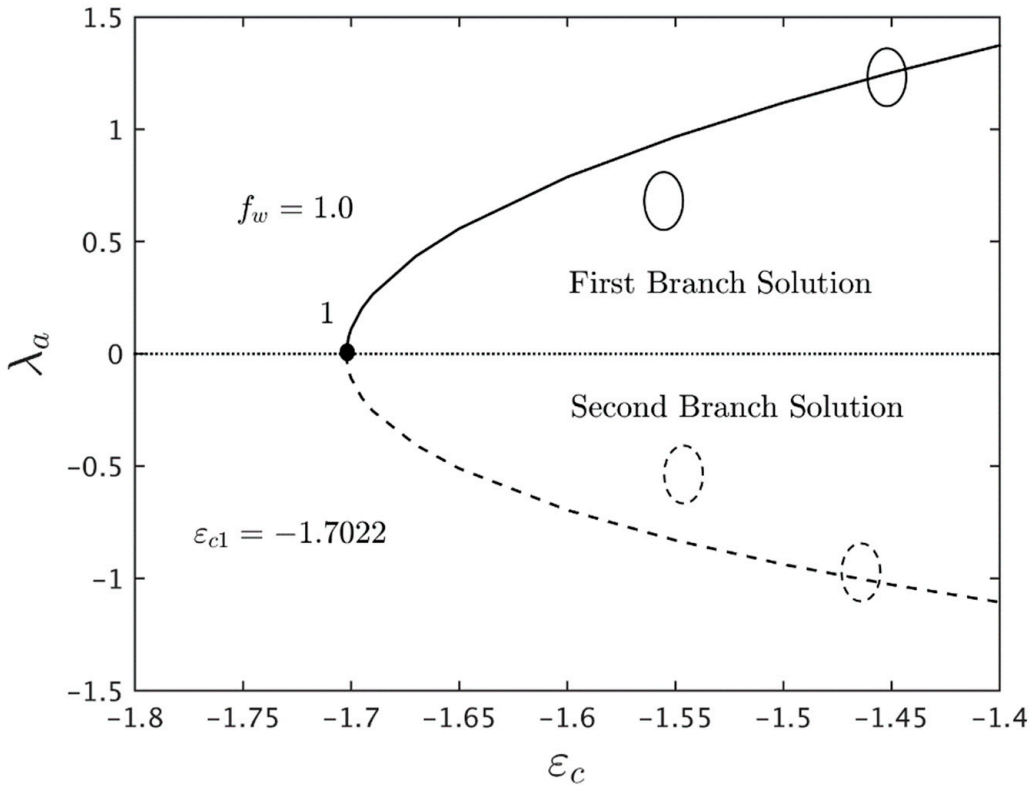

Figure 17. Eigenvalue λ_a for several values of ε_c.

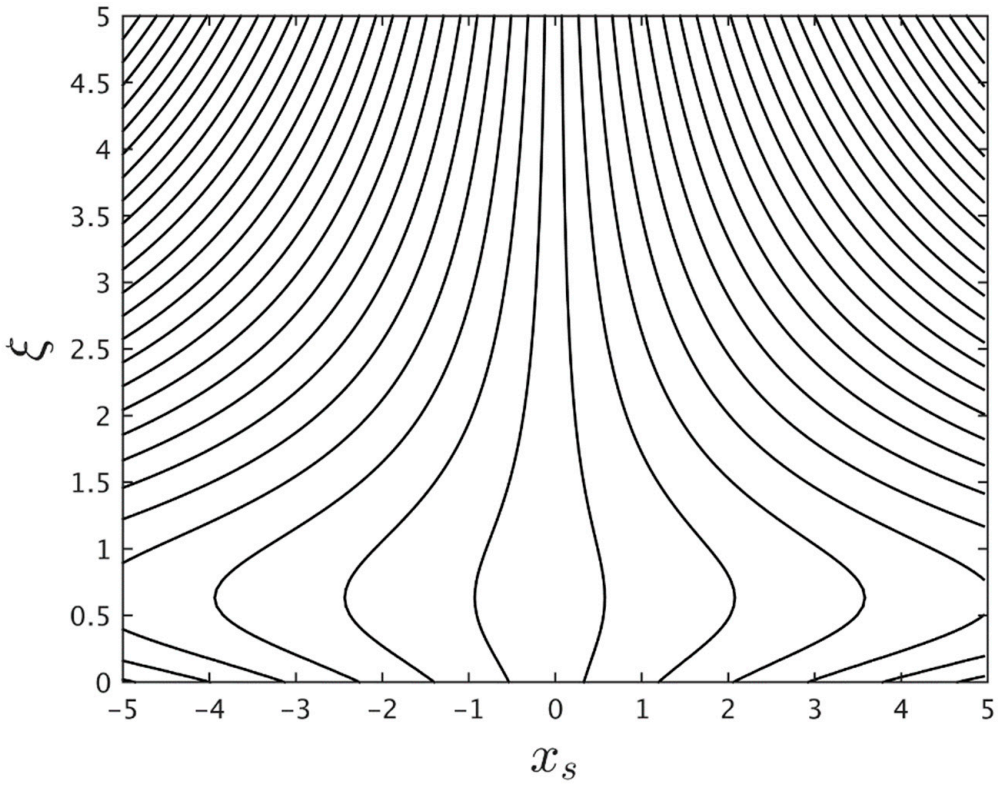

Figure 18. Plot of streamlines for the upper branch solution when $M_c = 0.5$.

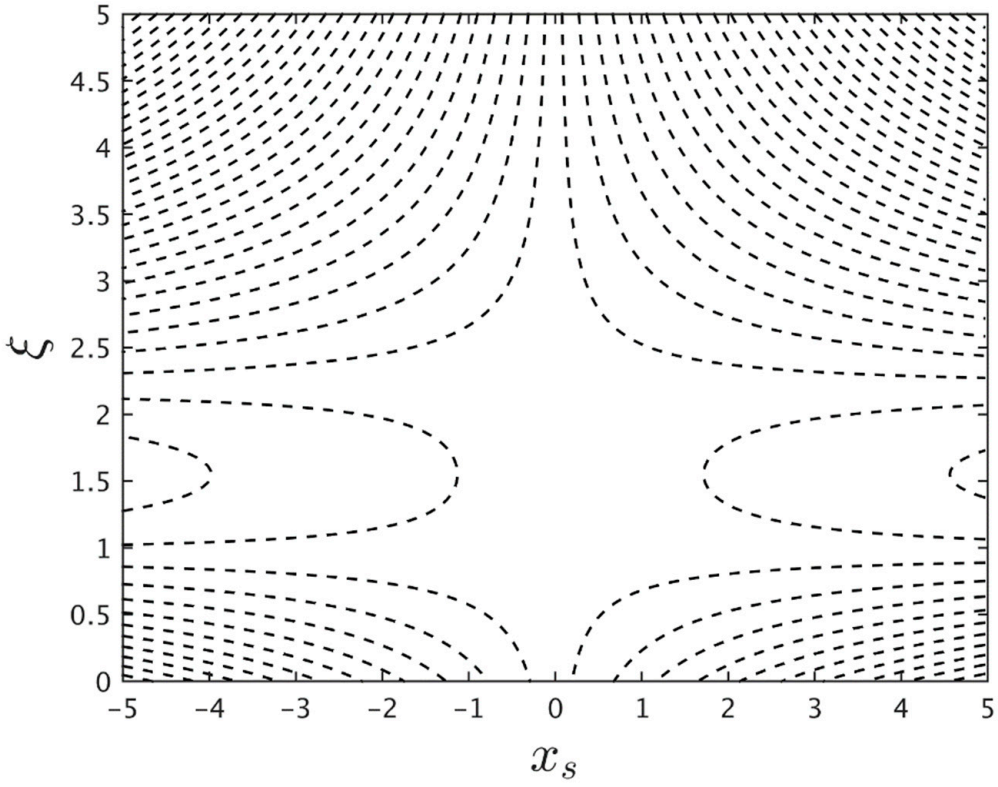

Figure 19. Plot of streamlines for the lower branch solution when $M_c = 0.5$.

Table 6 depicts the values of the heat transfer rate (HTR) for the FB as well as the SB solution with deviation in the larger selected values of N_r, A_s, B_s, φ_1, and φ_2 when $\varepsilon_c = -1.5$, $\gamma_c = -1.0$, $f_w = 1.0$, $M_c = 0.20$, $E_c = 0.5$, $m_s = 0.5$, and $K_c = 0.25$. The results

reveal that the values of the heat transfer enrich for both branches owing to the mounting values of the radiation parameter, φ_1 and φ_2. Also, the heat transfer inclines for the SBS and decays for the FBS in magnitude with larger impressions of the heat source factor ($A_s, B_s > 0$) while the pattern of the output values were reversed in both branches for the superior impacts of the heat sink factor ($A_s, B_s < 0$).

Figures 2–7 portray the variation of the reduced SSC (shear stress coefficient), the gradient of micro-rotation or CSC, and the heat transfer of the (water/Cu-Al_2O_3) hybrid nanofluid for the several values of f_w and M_c. It was found that multiple or double solutions (FB and SB results) happened for Equations (20)–(22) subject to the BCs (23) in the region of $\varepsilon > \varepsilon_c$, in which ε_c represents the bifurcation value of ε. Note that a unique solution exists for $\varepsilon = \varepsilon_c$, while no solutions exist when $\varepsilon < \varepsilon_c$. Additionally, from these graphs, it is clear that the output values of $|\varepsilon_c|$ upsurge as the requisite parameters f_w and M_c upsurge, indicating that these factors/parameters expand the range in which dual/double solutions can occur. Further evidence supports the idea that the inclusion of hybrid nanoparticles, the suction effect, the magnetic field, and the stretching sheet could slow the boundary layer separation (BLS), but the presence of the material parameter and the shrinking sheet could speed up the BLS. Also, for the FBS, the values of the HTR and CSC are consistently positive owing to the HT from the precise hot surface of the stretched/contracted sheet to the requisite cold fluid. The opposite pattern is noticed in the phenomenon of the SBS, i.e., the heat transfer rate and the couple stress coefficient become unavailable as $\varepsilon_c \to 0.55^+$ and $\varepsilon_c \to 0.55^-$.

The impression of the mass suction parameter f_w on the SSC, CSC, and HTR of the (water/Cu-Al_2O_3) hybrid nanofluid for the FB and SB solutions is presented in Figures 2–4, respectively. The outcomes display that the gradients (SSC, CSC, and HTR) boosted up for the FBS due to the higher values of f_w while it declines for the branch of second solutions. In addition, it is noticeable that the SSC values of the FBS are slightly higher and better than the values of CSC with higher impacts of the mass suction parameter as seen graphically in Figures 2 and 3. This behavior is due to the fact that the influence of the mass suction at the surface boundary of the stretched/shrinked surface slows down the hybrid nanofluid motion and escalates the shear stress and couple-stress coefficients at the surface of the vertical sheet. On the other hand, the rate of heat transmission developed as the magnitude of the mass transpiration parameter was boosted (see Figure 4). According to this fact, the thermal boundary layer thickness decelerates with larger impacts of the mass suction parameter, and as a response, the temperature distribution gradient of the sheet uplifts.

Figures 5–7 illustrate the impacts of the magnetic parameter M_c on the SSC, CSC, and HTR of the (water/Cu-Al_2O_3) hybrid nanofluid for the FB and SB solutions, respectively. In these graphs, it is initiated that the CSC and HTR improve in the FBS but decay in the SBS owing to the larger impacts of M_c while the SSC behaves increasingly for the FB solutions and a monotonic kind of behavior or a changeable behavior was followed in the same branch, moving away from the critical values for the larger effects of the magnetic field. Physically, by enlarging the values of the magnetic parameter, a force is produced which slows down the motion of fluid along the stretching/shrinking sheet and increases the convection of thermal energy by boosting the interactivity of the fluid particles which is known as the Lorentz force. According to this force, the speed of the hybrid nanoparticles of the fluid slows down. As a result, the shear stress and couple-stress coefficients are enlarged. Additionally, the gap among the curves for the FB is compared to the SB solutions as seen in Figures 5 and 6, and vice versa, for the heat transfer rate as graphically depicted in Figure 7. Furthermore, when the effects of magnetic field strength grow, the rate of heat transmission increases. This tendency results from the decreasing thermal boundary layer thickness caused by a growing magnetic field, which causes an intensification in the posited temperature gradient at the vertical sheet's surface.

The impacts of the solid nanoparticles volume fraction φ_1 and φ_2 on the shear stress coefficient (SSC), couple stress coefficient (CSC), and heat transfer rate for the double branch (FB and SB) solutions versus the mixed convection parameter γ_c are described

in Figures 8–10, respectively. These figures show that the heat transfer rate, shear stress, and couple-stress coefficients enrich for the first branch solutions due to the larger values of φ_1 and φ_2. Alternatively, the HTR declines for the SBS with higher impacts of φ_1 and φ_2 while the shear stress and couple-stress coefficients behave similarly to the FBS. Generally, there is a direct correlation between the volume percentage of nanoparticles and the temperature profiles. By increasing the volume percentage of nanoparticles, the thermal conductivity increases, which results in a monotonic development of the thermal boundary layer thickness and the temperature distributions. Due to this reason, the thermal conductivity rises as the volume percentage of nanomaterials increases, resulting in the thermal BLF and the HTR of the sheet. Furthermore, it is revealed that the two branches (FB and SB) solution is possible in the region when $\gamma > \gamma_c$, in which γ_c is the critical/bifurcation value of γ. Moreover, the outcome is not possible for the posited range $\gamma_c > \gamma$, while a unique or solo solution is initiated at the specific bifurcation point $\gamma = \gamma_c$. Besides, the magnitude of the gradients (SSC, CSC, and HTR) uplifts with the rise of the solid nanoparticles volume fraction φ_1 and φ_2. In other words, the absolute output numbers of $|\gamma_c|$ are revealed to be superior for larger values of the solid nanoparticles volume fraction φ_1 and φ_2 (see Figures 8–10). Hence, the impact of φ_1 and φ_2 upsurges the region of the mixed convection or buoyancy parameter for which the outcome is possible to exist. These plots additionally reveal that the bigger value of the hybrid nanoparticles slows down the BLS.

Figures 11–13 show the variation of the respective SSC, CSC, and HTR of the (water/Cu-Al_2O_3) hybrid nanofluid for the FB and SB solutions due to larger values of the material parameter K_c. Notably, it is evident from the Figures 11 and 12 that the shear stress initially declines and then upsurges for the FBS with a higher impact of material parameters, but the couple shear stress continuously decreases for the FBS. Whereas, for the branch of second solutions, the gradient of micro-rotation escalates due to larger values of K_c, while shear stress decelerates and behaves vice versa. On the other hand, the heat transfer decreases and increases for the branch of the first and second solutions, respectively, owing to the superior hammering of the parameter K_c (see Figure 13). In all three graphs, the gap was slightly lesser in both solution branches, therefore, we have to zoom in on the specific part where both solutions can meet or merge at a single point, called a bifurcation point γ_c. The bifurcation values for the distinct choices of K_c are shown by the small solid black balls and also numerally highlighted in the suggested plots. Additionally, the absolute values of $|\gamma_c|$ are smaller for the superior values of K_c. In this regard, the pattern of the outcomes indicates that the larger values of the material parameter speed up the level of the separation of the boundary layer.

The effects of the radiation parameter N_r on the temperature distribution profiles of the (water/Cu-Al_2O_3) hybrid nanofluid for both branches of solutions is graphically exemplified in Figure 14. From the graph, it is seen that both solution branches and the thickness of the TTBL boosted up as the value of the N_r was augmented. Moreover, the double branch (FB and SB) solutions asymptotically hold the boundary Conditions (23). Also, the gap in both solution curves is reasonable/understandable for the higher impacts of the radiation parameter. Physically, the thermal conductivity is improved by bigger values of the radiation parameter, which can lead to an increase in temperature distribution profiles as well as in the thickness of the thermal boundary layer.

Figures 15 and 16 designate the significance of the internal heat source factor $(A_s, B_s > 0)$ and heat sink constraint $(A_s, B_s < 0)$ on the temperature field curves of the (water/Cu-Al_2O_3) hybrid nanoparticles, respectively. In both graphs, the results were constructed/prepared for the branch of the first and second solutions. In addition, the outcome of both plots demonstrates that the profile of the temperature and the TTBL augment with the superior impacts of the internal heat source factor for the FBS as well as for the SBS, while it is reducing continuously with the internal heat sink factor. Generally, the reason this happens is because the heat source factor causes the system to absorb more energy as a result of heat, and, as a response, the temperature enriches (see Figure 15). On the other hand (see Figure 16), the

system did not receive a better level of heat (in the form of energy) owing to the requisite heat sink factor and, as a consequence, the temperature profile decelerated. Furthermore, the gap in both solution cases is looking similar to the rising value of the internal heat source/sink factors.

The temporal stability analysis was assumed to check the stability of the multiple or double-branch solutions. Thus, the smallest eigenvalue λ_a was calculated by solving the linear eigenvalue Problems (39)–(42) using the built-in code working in MATLAB. Figure 17 shows the minimum eigenvalue λ_a against the posited parameter ε_c. The first branch solution is represented by the positive eigenvalue, whereas the second branch solution is represented by the negative eigenvalues. It may be determined that the first-branch solution is stable and substantially more practicable than the second-branch solution, which is unstable and physically not acceptable. Furthermore, the streamlines pattern for the upper and lower branch solutions are represented in Figures 18 and 19 when $M_c = 0.5$. Outcomes show that for the branch of the top solution, the streamline pattern is simple curves and symmetric in the corresponding axial axis, however for the lower branch solution, the streamlines pattern is ambiguously complex and divided the flow into double regions.

6. Conclusions

The present study has explored the magnetohydrodynamic (MHD) and non-uniform heat source effects on the flow of micropolar hybrid nanofluid through stretchable/shrinkable permeable vertical sheet. With the aid of the similarity variables, the governing Equations (1)–(4) in PDEs form have been reduced to the similarity Equations (20)–(22) which are in the ODEs form. Then, these resulting ODEs are solved numerically by using the bvp4c solver in MATLAB. In addition, the eigenvalue Equations (39)–(42) are formulated to evaluate the stability of the outcomes by generating the eigenvalues for some sets of the physical parameter values. The numerical results are presented in the table and graphical forms. The findings from the numerical computational are concisely presented as follows:

- The mass suction parameter f_w and the magnetic parameter M_c contributes to enhancing the SSC and the CSC, as well as the heat transfer performance of the HN.
- Besides enhancing the skin friction and the couple stress coefficients, the added nanoparticles volume fraction φ_1 and φ_2 also improves the Nusselt number. This behavior is expected since the nanoparticles improve the thermal conductivity of the base fluid due to their synergic effect.
- Moreover, the material parameter K_c lowers the couple stress coefficient and heat transfer performance of the hybrid nanofluid, but the SSC is slightly increased with this parameter.
- The domain of the stretching/shrinking parameter ε_c is expanded for the larger mass suction parameter f_w and the magnetic parameter M_c. These behaviors are proven by looking at the critical points of the parameter where they are moving on the left side of the shrinking regions. Similar behavior is observed for the buoyancy parameter γ_c for some values of the material parameter K_c.
- The heat source parameter boosts the temperature profiles, and the opposite behavior is shown by the heat sink parameter for both the first and second solutions.
- According to the stability analysis, the eigenvalue obtained for the first solution is in positive values, while the negative values of the eigenvalues are shown in the second solution. These behaviors prove that the FBS is stable in the long run and vice versa.

The current observations can be utilized to lead future research in which the heat effect of system heating is assessed by taking into account different types of non-Newtonian hybrid nanofluids (Casson, third-grade, Williamson, Prandtl fluid, power-law fluid nanofluids). In addition, boundary conditions can be considered such as slip effects and convective boundary conditions to investigate the hybrid nanofluid flow.

Author Contributions: Conceptualization, A.M.A. and U.K.; methodology, S.M.E. and U.K.; software, S.M.E., A.M.A. and U.K.; validation, A.I., S.M.E., A.Z., U.K. and A.M.A.; formal analysis, A.Z., I.W., J.K.M., A.M.A. and N.A.; investigation, U.K., I.W., A.M.A., J.K.M. and A.I.; resources, N.A. and I.W.; data curation, J.K.M., N.A. and A.M.A.; writing—original draft preparation, A.I., A.Z., U.K., J.K.M. and N.A.; writing—review and editing, A.I., A.Z., J.K.M., I.W. and N.A.; visualization, A.Z. and S.M.E.; supervision, A.I.; project administration, S.M.E.; funding acquisition, S.M.E. All authors have read and agreed to the published version of the manuscript.

Funding: This work was partially funded by the research center of the Future University in Egypt, 2022.

Acknowledgments: The authors are thankful for the partial support of the Research Center of the Future University in Egypt, 2022.

Conflicts of Interest: The authors declare no conflict of interest.

References

1. Choi, S.U.S. Enhancing thermal conductivity of fluids with nanoparticles. In *Developments and Applications of Non-Newtonian Flows, FED*; Siginer, D.A., Wang, H.P., Eds.; ASME: New York, NY, USA, 1995; Volume 231/MD-66, pp. 99–105.
2. Lin, Y.; Zheng, L. Marangoni boundary layer flow and heat transferof copper-water nanofluid over a porous medium disk. *AIP Adv.* **2015**, *5*, 107225. [CrossRef]
3. Dogonchi, A.S.; Ganji, D.D. Thermal radiation effect on the Nanofluid buoyancy flow and heat transfer over a stretching sheet considering Brownian motion. *J. Mol. Liq.* **2016**, *223*, 521–527. [CrossRef]
4. Bhatti, M.M.; Abbas, T.; Rashidi, M.M. Entropy generation as a practical tool of optimisation for non-Newtonian nanofluid flow througha permeable stretching surface using SLM. *J. Comput. Des. Eng.* **2017**, *4*, 21–28.
5. Sheremet, M.A.; Cimpean, D.S.; Pop, I. Free convection in a partially heated wavy porous cavity filled with a nanofluid under the effects of Brownian diffusion and thermophoresis. *Appl. Therm. Eng.* **2017**, *113*, 413–418. [CrossRef]
6. Dogonchi, A.S.; Chamkha, A.J.; Seyyedi, S.M.; Ganji, D.D. Radiative nanofluid flow and heat transfer between parallel disks with penetrable and stretchable walls considering Cattaneo-Christov heat flux model. *Heat Transf. Asian Res.* **2018**, *47*, 735–753. [CrossRef]
7. Khan, U.; Zaib, A.; Ishak, A. Magnetic field effect on Sisko fluid flow containing gold nanoparticles through a porous curved surface in the presence of radiation and partial slip. *Mathematics* **2021**, *9*, 921. [CrossRef]
8. Gasmi, H.; Khan, U.; Zaib, A.; Ishak, A.; Eldin, S.M.; Raizah, Z. Analysis of mixed convection on two-phase nanofluid flow past a vertical plate in Brinkman-Extended Darcy porous medium with Nield conditions. *Mathematics* **2022**, *10*, 3918. [CrossRef]
9. Ghadikolaei, S.S.; Yassari, M.; Sadeghi, H.; Hosseinzadeh, K.; Ganji, D.D. Investigation on thermophysical properties ofTiO_2–Cu/H2O hybrid nanofluid transport dependent on shape factor in MHD stagnation point flow. *Powder Technol.* **2017**, *322*, 428–438. [CrossRef]
10. Sundar, L.S.; Sharma, K.V.; Singh, M.K.; Sousa, A.C.M. Hybrid nanofluids preparation, thermal properties, heat transfer andfriction factor—A review. *Renew. Sustain. Energy Rev.* **2017**, *68*, 185–198.
11. Jamaludin, A.; Naganthran, K.; Nazar, R.; Pop, I. MHD mixed convection stagnation-point flow of Cu-Al_2O_3/water hybrid nanofluid over a permeable stretching/shrinking surface with heat source/sink. *Eur. J. Mech. B Fluids* **2020**, *84*, 71–80. [CrossRef]
12. Khashi'ie, N.S.; Arifin, N.M.; Pop, I. Mixed convective stagnation point flow towards a vertical Riga plate in hybrid Cu-Al_2O_3/water nanofluid. *Mathematics* **2020**, *8*, 912. [CrossRef]
13. Waini, I.; Ishak, A.; Pop, I. Flow and heat transfer of a hybrid nanofluid past a permeable moving surface. *Chin. J. Phys.* **2020**, *66*, 606–619. [CrossRef]
14. Abu Bakar, S.; Md Arifin, N.; Khashi'ie, N.S.; Bachok, N. Hybrid Nanofluid Flow over a Permeable Shrinking Sheet Embedded in a Porous Medium with Radiation and Slip Impacts. *Mathematics* **2021**, *9*, 878. [CrossRef]
15. Salawu, S.O.; Obalalu, A.M.; Shamshuddin, M.D. Nonlinear solar thermal radiation efficiency and energy optimization for magnetized hybrid Prandtl–Eyring nanoliquid in aircraft. *Arabian J. Sci. Eng.* **2022**. [CrossRef]
16. Eringen, A. Theory of micropolar fluids. *J. Math. Mech.* **1966**, *16*, 1–18. [CrossRef]
17. Ishak, A.; Lok, Y.Y.; Pop, I. Stagnation-point flow over a shrinking sheet in a micropolar fluid. *Chem. Eng. Commun.* **2010**, *197*, 1417–1427. [CrossRef]
18. Yacob, N.A.; Ishak, A. Stagnation point flow towards a stretching/shrinking sheet in a micropolar fluid with a convective surface boundary condition. *Can. J. Chem. Eng.* **2012**, *90*, 621–626. [CrossRef]
19. Soid, S.K.; Ishak, A.; Pop, I. MHD stagnation-point flow over a stretching/shrinking sheet in a micropolar fluid with a slipboundary. *Sains Malays.* **2018**, *47*, 2907–2916. [CrossRef]
20. El-Aziz, M.A. Viscous dissipation effect on mixed convection flow of a micropolar fluid over an exponentially stretching sheet. *Can. J. Phys.* **2009**, *87*, 359–368. [CrossRef]
21. Turkyilmazoglu, M. Mixed convection flow of magnetohydrodynamic micropolar fluid due to a porous heated/cooled deformable plate: Exact solutions. *Int. J. Heat Mass Transf.* **2017**, *106*, 127–134. [CrossRef]

22. Ramadevi, B.; Anantha Kumar, K.; Sugunamma, V.; Ramana Reddy, J.V.; Sandeep, N. Magnetohydrodynamic mixed convective flow of micropolar fluid past a stretching surface using modified fourier's heat flux model. *J. Therm. Anal. Calorim.* **2020**, *139*, 1379–1393. [CrossRef]
23. Rafique, K.; Alotaibi, H.; Nofal, T.A.; Anwar, M.I.; Misiran, M.; Khan, I. Numerical solutions of micropolar nanofluid over an inclined surface using Keller box analysis. *J. Math.* **2020**, *2020*, 1–13. [CrossRef]
24. Sajid, T.; Jamshed, W.; Shahzad, F.; Eid, M.R.; Alshehri, H.M.; Goodarzi, M.; Akgül, E.K.; Nisar, K.S. Micropolar fluid past a convectively heated surface embedded with nth order chemical reaction and heat source/sink. *Phys. Scr.* **2021**, *96*, 104010. [CrossRef]
25. Kausar, M.S.; Hussanan, A.; Waqas, M.; Mamat, M. Boundary layer flow of micropolar nanofluid towards a permeable stretching sheet in the presence of porous medium with thermal radiation and viscous dissipation. *Chin. J. Phys.* **2022**, *78*, 435–452. [CrossRef]
26. Attia, H.A. Stagnation point flow and heat transfer of a micropolar fluid with uniform suction or blowing. *J. Braz. Soc. Mech. Sci. Eng.* **2008**, *30*, 51–55. [CrossRef]
27. Awaludin, I.S.; Weidman, P.D.; Ishak, A. Stability analysis of stagnation-point flow over a stretching/shrinking sheet. *AIP Adv.* **2016**, *6*, 045308. [CrossRef]
28. Sadiq, M.A. MHD stagnation point flow of nanofluid on a plate with anisotropic slip. *Symmetry* **2019**, *11*, 132. [CrossRef]
29. Zainal, N.A.; Nazar, R.; Naganthran, K.; Pop, I. Unsteady stagnation point flow of hybrid nanofluid past a convectively heated stretching/shrinking sheet with velocity slip. *Mathematics* **2020**, *8*, 1649. [CrossRef]
30. Mahmood, Z.; Ahamm, N.A.; Alhazmi, S.E.; Khan, U.; Bani-Fwaz, M.Z. Ternary hybrid nanofluid near a stretching/shrinking sheet with heat generation/absorption and velocity slip on unsteady stagnation point flow. *Int. J. Modern Phys. B* **2022**, *36*, 2250209. [CrossRef]
31. Pal, D.; Mandal, G. Thermal radiation and MHD effects on boundary layer flow of micropolar nanofluid past a stretching sheet with non-uniform heat source/sink. *Int. J. Mech. Sci.* **2017**, *126*, 308–318. [CrossRef]
32. Sharma, K.; Gupta, S. Viscous dissipation and thermal radiation effects in MHD flow of Jeffrey nanofluid through impermeable surface with heat generation/absorption. *Nonlinear Eng.* **2017**, *6*, 153–166. [CrossRef]
33. Jamaludin, A.; Nazar, R.; Pop, I. Mixed convection stagnation-point flow ofa nanofluid past a permeable stretching/shrinking sheet in the presence of thermal radiation and heat source/sink. *Energies* **2019**, *12*, 788. [CrossRef]
34. Khan, U.; Zaib, A.; Ishak, A.; Eldin, S.M.; Alotaibi, A.M.; Raizah, Z.; Waini, I.; Elattar, S.; Abed, A.M. Features of hybridized AA7072 and AA7075 alloys nanomaterials with melting heat transfer past a movable cylinder with Thompson and Troian slip effect. *Arab. J. Chem.* **2022**, 104503. [CrossRef]
35. Khan, U.; Zaib, A.; Ishak, A.; Elattar, S.; Eldin, S.M.; Raizah, Z.; Waini, I.; Waqas, M. Impact of irregular heat sink/source on the wall Jet flow and heat transfer in a porous medium induced by a nanofluid with slip and buoyancy effects. *Symmetry* **2022**, *14*, 1312. [CrossRef]
36. Sheremet, M.A.; Pop, I.; Bachok, N. Effect of thermal dispersion on transient natural convection in a wavy-walled porous cavity filled with a nanofluid: Tiwari and Das' nanofluid model. *Int. J. Heat Mass Transf.* **2016**, *92*, 1053–1060. [CrossRef]
37. Pang, C.; Jung, J.Y.; Kang, Y.T. Aggregation based model for heat conduction mechanism in nanofluids. *Int. J. Heat Mass Transf.* **2014**, *72*, 392–399. [CrossRef]
38. Ebrahimi, A.; Rikhtegar, F.; Sabaghan, A.; Roohi, E. Heat transfer and entropy generation in a microchannel with longitudinal vortex generators using nanofluids. *Energy* **2016**, *101*, 190–201. [CrossRef]
39. Ishak, A.; Nazar, R.; Pop, I. The Schneider problem for a micropolar fluid. *Fluid Dyn. Res.* **2006**, *38*, 489. [CrossRef]
40. Ishak, A.; Nazar, R.; Pop, I. Mixed convection stagnation point flow of a micropolar fluid towards a stretching sheet. *Meccanica* **2008**, *43*, 411–418. [CrossRef]
41. Zaib, A.; Khan, U.; Khan, I.; Seikh, A.H.; Sherif, E.S.M. Entropy generation and dual solutions in mixed convection stagnation point flow of micropolar Ti6Al4V nanoparticle along a Riga surface. *Processes* **2019**, *8*, 14. [CrossRef]
42. Oztop, H.F.; Abu-Nada, E. Numerical study of natural convection in partially heated rectangular enclosures filled with nanofluids. *Int. J. Heat Fluid Flow* **2008**, *29*, 1326–1336. [CrossRef]
43. Khan, U.; Zaib, A.; Ishak, A.; El-Sayed Sherif, M.; Waini, I.; Chu, Y.-M.; Pop, I. Radiative mixed convective flow induced by hybrid nanofluid over a porous vertical cylinder in a porous media with irregular heat sink/source. *Case Stud. Therm. Eng.* **2022**, *30*, 101711. [CrossRef]
44. Merkin, J.H. On dual solutions occurring in mixed convection in a porous medium. *J. Eng. Math.* **1986**, *20*, 171–179. [CrossRef]
45. Weidman, P.D.; Kubitschek, D.G.; Davis, A.M.J. The effect of transpiration on self-similar boundary layer flow over moving surfaces. *Int. J. Eng. Sci.* **2006**, *44*, 730–737. [CrossRef]
46. Harris, S.D.; Ingham, D.B.; Pop, I. Mixed convection boundary-layer flow near the stagnation points on a vertical surface in a porous medium: Brinkman model with slip. *Transp. Porous Media* **2009**, *77*, 267–285. [CrossRef]
47. Shampine, L.F.; Kierzenka, J.; Reichelt, M.W. Solving boundary value problems for ordinary differential equations in MATLAB with bvp4c. *Tutor. Notes* **2000**, *2000*, 1–27.
48. Shampine, L.F.; Gladwell, I. *Thompson. S. Solving ODEs with Matlab*; Cambridge University Press: Cambridge, UK, 2003.

49. Shah, S.H.A.M.; Suleman, M.; Khan, U. Dual solution of MHD mixed convection flow and heat transfer over a shrinking sheet subject to thermal radiation. *Partial. Differ. Equ. Appl. Math.* **2022**, *6*, 100412. [CrossRef]
50. Lok, Y.Y.; Amin, N.; Campean, D.; Pop, I. Steady mixed convection flow of a micropolar fluid near the stagnation point on a vertical surface. *Int. J. Numer. Methods Heat Fluid Flow* **2005**, *15*, 654–670. [CrossRef]